

Photocatalytic Degradation of Methylene Blue Using N-Doped ZnO/Carbon Dot (N-ZnO/CD) Nanocomposites Derived from Organic Soybean

Dinda Gusti Ayu, Saharman Gea,* Andriyani, Dewi Junita Telaumbanua, Averroes Fazlur Rahman Piliang, Mahyuni Harahap, Zhihao Yen, Ronn Goei, and Alfred Iing Yoong Tok



Cite This: *ACS Omega* 2023, 8, 14965–14984



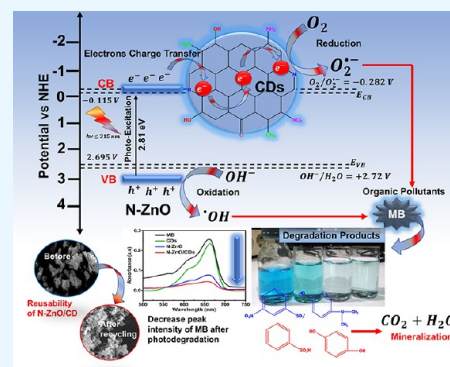
Read Online

ACCESS |

Metrics & More

Article Recommendations

ABSTRACT: This study reports on successful synthesis of carbon dots (CDs), nitrogen-doped zinc oxide (N-ZnO), and N-ZnO/CD nanocomposites as photocatalysts for degradation of methylene blue. The first part was the synthesis of CDs utilizing a precursor from soybean and ethylenediamine as a dopant by a hydrothermal method. The second part was the synthesis of N-ZnO with urea as the nitrogen dopant carried out by a calcination method in a furnace at 500 °C for 2 h in an N₂ atmosphere (5 °C min⁻¹). The third part was the synthesis of N-ZnO/CD nanocomposites. The characteristics of CDs, N-ZnO, and N-ZnO/CD nanocomposites were analyzed through Fourier transform infrared (FTIR), UV–vis absorbance, photoluminescence (PL), high-resolution transmission electron microscopy (HR-TEM), X-ray diffraction (XRD), thermal gravimetry analysis (TGA), field-emission scanning electron microscopy energy-dispersive spectroscopy (FESEM EDS), X-ray photoelectron spectroscopy (XPS), and Brunauer–Emmett–Teller (BET) analysis. Based on the HR-TEM analysis, the CDs had a spherical shape with an average particle size of 4.249 nm. Meanwhile, based on the XRD and HR-TEM characterization, the N-ZnO and N-ZnO/CD nanocomposites have wurtzite hexagonal structures. The materials of N-ZnO and N-ZnO/CD show increased adsorption in the visible light region and low energy gap E_g . The E_g values of N-ZnO and N-ZnO/CDs were found to be 2.95 and 2.81 eV, respectively, whereas the surface area (S_{BET}) values 3.827 m² g⁻¹ (N-ZnO) and 3.757 m² g⁻¹ (N-ZnO/CDs) belonged to the microporous structure. In the last part, the photocatalysts of CDs, N-ZnO, and N-ZnO/CD nanocomposites were used for degradation of MB (10 ppm) under UV-B light irradiation pH = 7.04 (neutral) for 60 min at room temperature. The N-ZnO/CD nanocomposites showed a photodegradation efficiency of 83.4% with a kinetic rate of 0.0299 min⁻¹ higher than N-ZnO and CDs. The XRD analysis and FESEM EDS of the N-ZnO/CDs before and after three cycles confirm the stability of the photocatalyst with an MB degradation of 58.2%. These results have clearly shown that the N-ZnO/CD nanocomposites could be used as an ideal photocatalytic material for the decolorization of organic compounds in wastewater.



1. INTRODUCTION

The pharmaceuticals, plastics, paints, textiles, pulp, food, and agriculture-related industries used a large amount of chemicals including organic dyes in their production process.¹ When organic dyes are dissolved in water at the concentration ≥ 1 mg L⁻¹, they become harmful pollutants to the environment and cause health problems to living organisms.^{2,3} The organic dye substances are chemically stable, so they are difficult to degrade.⁴ Methylene blue (C₁₆H₁₈CN₃SCl) is a heterocyclic aromatic and a type of cationic compound used mainly as a coloring agent in the industries. If liquid waste containing methylene blue is released into the environment, the environment will become contaminated, which causes declining water quality.⁵ These toxic materials harm human health. They may cause skin and eye irritations and interfere with the working

systems of the kidneys, liver, brain, reproduction system, and central nervous system.⁶

Many methods have been investigated for effective removal of methylene blue, such as extraction, ozonation, ion flotation, Fenton process, sonolysis, ultrafiltration, coagulation using chemicals, adsorption, flocculation, oxidation, and photocatalysis.^{7–11} Among the available methods, photocatalysis is generally preferred because the process is simpler and

Received: November 25, 2022

Accepted: March 30, 2023

Published: April 17, 2023



environmentally friendly, especially with the utilization of sunlight as the energy source. There are several important parameters to be considered in the photocatalysis process, such as bandgap energy, effective surface area, light energy absorption characteristic of the photocatalytic materials and the operating intensity, temperature, and pH of the photocatalytic degradation.¹² The ZnO semiconductor is one of the potential photocatalyst materials; ZnO is chemically and physically stable with high biocompatibility.¹³ However, ZnO has a wide bandgap energy of 3.37 eV; it has quick recombination of charge carriers and comparatively low charge separation, which leads to nonoptimal photocatalytic performance.¹⁴ Therefore, the addition of dopants and the introduction of supporting materials such as nanocarbons in the preparation of semiconductor nanocomposites can improve the efficacy of ZnO as a photocatalytic material.^{15,16}

Nitrogen doping and the addition of nanocarbon supporting materials are proved to be an effective way to reduce the energy gap of the semiconductor photocatalyst and the recombination rate of electron (e^-) and hole (h^+) pairs can be controlled so that the photocatalytic process becomes more effective.¹⁷ Recently, the addition of nanocarbon materials has been widely proposed to support photocatalytic performance. Kumar et al. studied green catalyst technology for water treatment using agricultural waste as a source to synthesize green nanoparticles (NPs). Photocatalyst-based green NPs are considered to be the right green, easy, and low-cost technology for treating organic pollutants in water.¹⁸ Hassani et al. have explored a carbon-based catalyst (carbocatalysts), i.e., reduced graphene oxide rGO in nanocomposites CoFe_2O_4 -rGO to activate peroxymonosulfate (PMS) for degradation of bisphenol A (BPA) by UVA-LED irradiation, where 99.5% BPA can be eliminated during 30 min. A high degradation activity is supported by rGO. rGO has a good specific surface area, unique surface chemistry, adsorption capacity, and electrocatalytic properties, so rGO can be a candidate for catalytic oxidation toward the activation of PMS.¹⁹ In addition, one of the green nanoparticle materials that can be utilized as a carbocatalyst is carbon dots (CDs). CDs have abundant sources of precursors such as agricultural products or waste, making these more environmentally friendly. In addition, CDs have several advantages, such as having the ability to adsorb visible rays, abundant electron donors and acceptors, strong photoluminescence (PL), photostability, and good solubility in water.^{20–24}

The use of dopants and the addition of nanocarbon supporting materials have been widely studied. Zhou et al. reported a comparison of the photocatalytic activity of ZnO nanorod cores, (ZnO/C) core-shell, and (ZnO/C/CdS) nanocables to degrade rhodamine B (RhB) solution (concentration 5 mg L^{-1}). After irradiation, the visible light of the Xe 500 lamp with a 420 nm cutoff filter for 60 min showed degradation results of 32.4, 58.3, and 90.7%, respectively. There is improved photocatalyst performance of the ZnO nanorod material in the presence of a carbon (C) shell and cadmium sulfide (CdS) NPs. Amorphous carbon layers on the surface of ZnO nanorods have good adsorption ability so that more photon energy can be absorbed, and the photocatalyst activity is also increased. CdS NPs function in the charge separation and transport process. This is useful for increasing the quantity of photogenerated costs.²⁵ On the other hand, Hassani et al. also studied the integration of mesoporous graphitic carbon nitride (mpg- C_3N_4) with silver (Ag) onto ZnO nanowires (NWs) formed by electrochemical anodization of Zn plate (mpg- C_3N_4 /Ag/ZnO

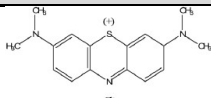
NWs/Zn) composites for photodegradation of direct orange 26 (DO26) with a degradation efficiency of 94% under 250 W mercury lamp illumination in 120 min reaction time. The combination of mpg- C_3N_4 and Ag on ZnO NWs/Zn is a strategy to increase the degradation activity of ZnO, because mpg- C_3N_4 with a porous structure can act as active adsorptive sites for adsorption of DO26 onto the surface of the photocatalyst and Ag has an important role in promoting (e^-) and (h^+) pairs, which are beneficial to accelerating the separation of charge and prevent recombination of (e^-/h^+) pairs.²⁶ However, the use of metal ion dopants such as CdS or Ag has low biocompatibility and limited metal sources and is feared to threaten the environment and human health. A workable solution is to use nonmetallic ions such as nitrogen. Prabakaran and Pillay have synthesized nitrogen-doped ZnO, which exhibits an MB photodegradation activity of 98.6% under UV light 250 W for 80 min.²⁷ In addition, Atchudan et al. have synthesized nitrogen-doped CD-adorned ZnO (N-CDs/ZnO) nanocomposites used as photocatalysts to degrade MB solution under UV light irradiation for 60 min; the results of this study show that the photodegradation activity of N-CDs/ZnO reaches 99%, higher than that of ZnO nanoparticles, which is 75%. N-CDs function as optically active centers that are fully responsible for the UV light absorption process.²⁸ Liang et al. have also studied the results of research about material cationic carbon quantum dots (L-CQDs)/ZnO composites to degrade phenol solution (concentration 10 ppm) under visible light by using a 500 W Xe lamp for 5.5 h. L-CQDs can completely degrade phenol 60% higher compared to ZnO pure. L-CQDs serve as an excellent sensitizer to visible-light response. From some of these studies, it is known that the use of dopant N and CDs in photocatalysts is useful for further degradation studies.

Motivated from some of these leading studies mentioned above, this study aims to report the preparation of N-doped ZnO/CD nanocomposites, where the CDs were obtained from an organic soybean source. The work could be divided into several parts, i.e., the synthesis of CDs, N-ZnO nanoparticles, and N-ZnO/CD nanocomposites. The first part is the synthesis of CDs by using biomass soybean through a hydrothermal method. Soybean contains proteins (38–40%), carbohydrates (30%), and fats (18%), which make them suitable as the precursor for CDs.²⁹ As a supporting material in the redox process of photocatalytic degradation MB, the activity of CDs needs to be optimized through the modification of the structure using nonmetallic doping.³⁰ The modification of CDs was carried out by introducing the N dopant from ethylenediamine (EDA) at different concentration levels, such as 5, 10, and 15% V/V. The second part was the synthesis of N-ZnO nanoparticles through heat treatment of zinc oxide powder with urea as the N dopant agent. The third part was the synthesis of N-ZnO/CD nanocomposites, which was carried out via a facile one-step synthesis method at 2:1 concentration ratio of N-ZnO and CDs. This study observed the effect of the N dopant onto ZnO and CDs materials onto the N-ZnO surface structure. The fourth part used materials CDs, N-ZnO nanoparticles, and N-ZnO/CD nanocomposites as photocatalysts in the photodegradation of MB (concentration 10 ppm) under UV light irradiation using a UV-B lamp 75 W for 60 min at room temperature. The present study demonstrates the impact of pH on decolorization of MB and a cyclic test to realize the stability and reusability of the N-ZnO/CDs photocatalyst.

2. EXPERIMENTAL DETAILS

2.1. Materials and Reagents. Soybean powder was obtained from a market in Medan, North Sumatra, Indonesia. Deionized water 0.8 $\mu\text{S}/\text{cm}$ was produced by PT PRINCO. ZnO (CAS-No: 1314-13-2), $\text{C}_2\text{H}_8\text{N}_2$ (CAS-No: 07-15-3), $\text{CH}_4\text{N}_2\text{O}$ (CAS-No: 57-13-6), H_2SO_4 , and NaOH (CAS-No: 1310-73-2) were purchased from Sigma-Aldrich. Methylene blue (C.I. 52,015), ethanol 70%, and UV-B lamp 75 W were supplied by a local supplier in Medan, North Sumatra, Indonesia. The physicochemical properties of MB are presented in Table 1. The reagents were used without further purification.

Table 1. Physicochemical Properties of Methylene Blue

Chemical structure	Molecular formula	M_w (g mol^{-1})	λ_{max} (nm)	Chemical class
	$\text{C}_{16}\text{H}_{18}\text{CN}_3\text{SCl}$	319.9	670	Basic

2.2. Synthesis of CDs. The synthesis of CDs was carried out by a hydrothermal method. In the first step, 25 g of soybean powder was mixed with 100 mL of deionized water and filtered. The filtrate was collected. Then, 50 mL of soybean filtrate was stirred at 350 rpm for 20 min until homogeneous. Next, the soybean filtrate was put into 100 mL autoclave and heated at 180 $^{\circ}\text{C}$ for 8 h. In the second step, 50 mL of soybean filtrate adding EDA with different concentrations, such as 5, 10, and 15%V/V, was added. After that, all three mixtures with different EDA concentrations were stirred at 350 rpm for 40 min to disperse EDA into the solution. Each of the samples was put into a 100 mL autoclave and heated at 180 $^{\circ}\text{C}$ for 8 h. The mixture was centrifuged at 5500 rpm for 60 min to separate the solids from the solution. The CDs in liquid and solids were stored in a dark

container for further use and characterization purposes. A schematic of the synthesis of CDs by a hydrothermal method is shown in Figure 1a.

2.3. Synthesis of Nitrogen-Doped ZnO. The synthesis of nitrogen-doped ZnO (N-ZnO) nanoparticles was carried out using the calcination process with some modification in the source of the ZnO material.³¹ First, 1 g of ZnO was dissolved in 15 mL of ethanol and stirred at 350 rpm for 30 min until a homogeneous solution was formed. Then, 0.6 g of urea was added to the solution and stirred at 350 rpm for 2 h to disperse urea into the solution. Next, the mixture was dried at 50 $^{\circ}\text{C}$. The dried mixture was calcined in the gas (N_2) at 500 $^{\circ}\text{C}$ for 2 h at 5 $^{\circ}\text{C min}^{-1}$ heating rate. N-ZnO was stored in a dark container for further use and characterization purposes. A schematic of the synthesis of N-ZnO by a calcination process is shown in Figure 1b.

2.4. Synthesis of N-ZnO/CD Nanocomposites. The synthesis of N-ZnO/CD nanocomposites was carried out using a facile one-step method, modifying the concentration ratios of two material components.³² First, 25 μL of CDs solution was mixed with 50 mg of N-ZnO, dispersed in 10 mL of ethanol, and stirred at 350 rpm for 30 min at room temperature, and then the mixture was sonicated in an ultrasonic bath for 2 h. Finally, N-ZnO/CD nanocomposites produced were dried and stored in a dark container for further use and characterization purposes. A schematic of the synthesis of N-ZnO/CD nanocomposites is shown in Figure 1c.

2.5. Photodegradation of Methylene Blue. Photocatalytic activity of CDs, N-ZnO nanoparticles, and N-ZnO/CD nanocomposites in degrading 10 ppm (10 mg L^{-1}) MB was analyzed under UV lamp (75 W, UV-B, $\lambda_{\text{max}} = 315$ nm, Nomoy Pet, China) light irradiation for 60 min. 5 mg of each of the photocatalyst materials was suspended in MB solution. Then, the solution was allowed to stand in a dark place for 1 h to ensure that the reactants would reach adsorption and desorption equilibrium on the surface of the catalyst.³³ All experiments were

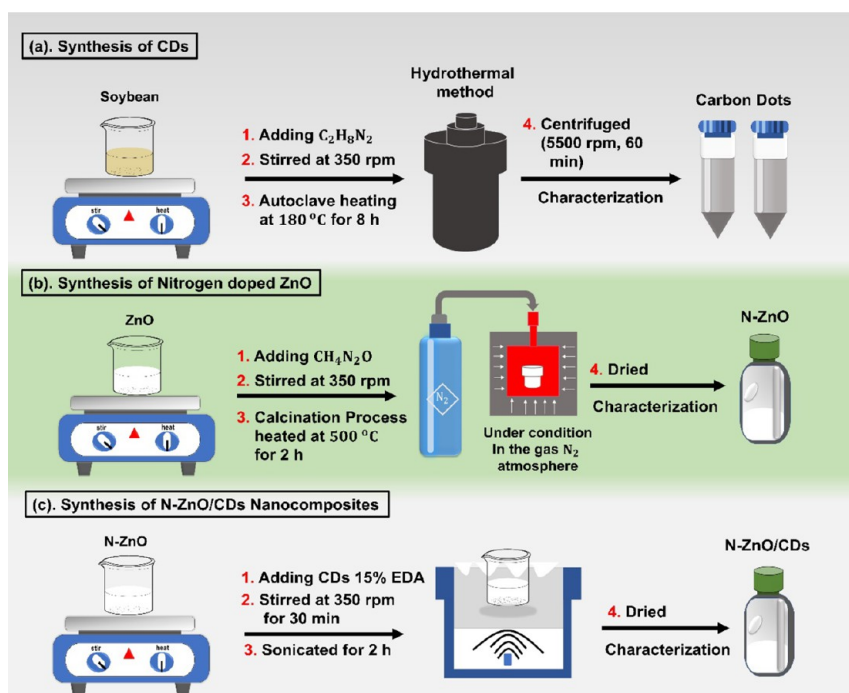


Figure 1. Schematic of the preparation of the photocatalyst material of CDs (a), N-ZnO nanoparticles (b), and N-ZnO/CD nanocomposites (c).

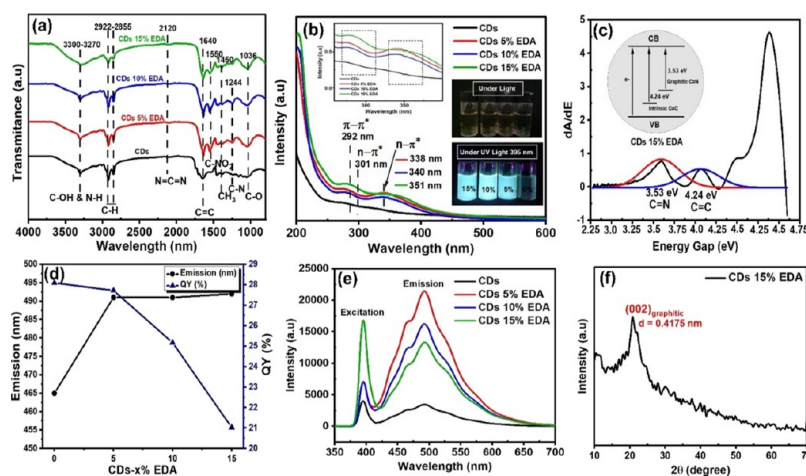


Figure 2. Analysis result characteristic of CDs, FTIR (a), UV-vis (b) (photograph of fluorescent CDs under UV lamp 365 nm, courtesy of Dinda Gusti Ayu. Copyright 2022), energy gap (c), quantum yield vs emission (d), photoluminescence (e), and XRD (f).

monitored in a chamber of dimensions 60 cm length, 60 cm width, and 45 cm height, and the distance of UV lamp with MB was 17 cm. The experiments were evaluated in pH 7.04 of the MB solution, for those experiments where the initial value was adjusted to alkaline and acidic conditions, an appropriate amount of NaOH and H₂SO₄ (0.1 M) was added and recorded with a pH meter (ATC, China). The absorbance intensity at the absorbance of 670 nm of each sample was measured using UV-vis spectroscopy to determine the photodegradation rate and MB concentration after the photocatalysis process as shown in eqs 1 and 2.

$$\text{Decolorization (\%)} = \left[1 - \frac{A_t (670 \text{ nm})}{A_0 (670 \text{ nm})} \right] \times 100 \quad (1)$$

$$\text{Concentration } (C_t) = \left[\frac{A_t (670 \text{ nm})}{A_0 (670 \text{ nm})} \right] \times C_0 (10 \text{ ppm}) \quad (2)$$

where C_0 is the initial concentration (concentration MB = 10 ppm), C_t is the concentration at time t , and A_0 and A_t are initials of MB absorbance before and after t minutes of irradiation.

2.6. Characterization Methodology and Performance Evaluation. The analysis of the component functional groups of the materials was performed using Fourier transform infrared (FTIR) spectroscopy in the range of 4000–500 cm^{−1}, Agilent Cary. The UV-vis absorbance spectra of the materials were obtained using a UV-vis spectrophotometer (Janway 7135) in the range of 200–800 nm. The PL spectra of the materials were obtained using a PL (USB2 + F00050 spectrophotometer with 1000 fluorescent). The crystal structure of the materials was characterized using an X-ray diffractometer (Rigaku XRD, $\lambda\text{Cu} - K\alpha = 1.5406 \text{ \AA}$). The surface morphology of the materials was observed with a field emission scanning electron microscope (FESEM) Thermo Scientific Quattr S equipped with energy-dispersive X-Ray spectroscopy (EDS) and FESEM JEOL 7600F at 20 kV accelerating voltage with oxford instruments EDX. Thermal gravimetry analysis (TGA) of the N-ZnO was performed using a Q500 thermogravimetric analyzer in 30–900 °C temperature range and at a heating rate of 10 °C min^{−1}. Particle size and lattice distance materials were obtained using high-resolution transmission electron microscopy (JEOL 2100F HR-TEM operating at 200 kV accelerating voltage). The surface

chemistry of materials was characterized using X-ray photoelectron spectrophotometry (XPS, Al-K α excitation source $h\nu = 1486.71 \text{ eV}$, Shimadzu Kratos Axis Supra). The specific analysis surface area of N-ZnO and NZnO/CDs was observed with Brunauer–Emmett–Teller (BET), and the pore size distribution was fitted with the Barrett–Joyner–Halenda (BJH) N₂ adsorption isotherm at 77 K Quanta chrome Nova 4200e.

3. RESULTS AND DISCUSSION

3.1. Characteristics of CDs. The characteristics of CDs with the varying concentrations of 5, 10, and 15%V/V EDA are presented in Figure 2. The FTIR spectrum of CDs is shown in Figure 2a. In the hydrothermal process, the precursor underwent several stages, such as carbonization, dehydration, polymerization, aromatization (ring formation), and formation of surface groups of CDs. These processes certainly depend on the composition of the precursors and the dopant agent used.³⁴ The presence of a carbon C=X core and several C–X functional groups in the structure affected the optical properties of the resulting CDs. CDs nondopant and CDs with different dopant concentrations, such as 5, 10, and 15%V/V EDA, showed peak characteristics at 3300, 2922, 1640, 1450, and 1036 cm^{−1} wavenumbers indicating the presence of C–OH (stretching vibration), C–H (bending vibration), C=C (bending vibration), CH₃ (bending vibration), and C–O (bending vibration), respectively.³⁵ CDs with varying dopant concentrations have the presence of C–NO₂ (bending) at 1550 cm^{−1}, which indicated the surface passivation of the EDA compound.³⁶ Wavenumbers 3270, 2120, and 1244 cm^{−1} representing N–H (stretching vibration), N=C=N (stretching vibration), and C–NH–C (stretching vibration) groups indicated the doping effect of the amide compounds from the soybean precursor.³⁷ The synthesized CDs from soybean as a precursor and EDA as a doping agent possess hydroxyl groups, amines, and amide functional groups on their surface.

The optical properties of CDs were analyzed by using UV-vis spectroscopy. The purpose of this analysis was to determine the absorbance range of CDs. The UV-vis absorbance spectrum of CDs and CDs with the varying dopant EDA samples is shown in Figure 2b. CDs generally showed an absorption peak characteristic between 220 and 480 nm in the UV and visible light regions.³⁸ The CDs synthesized from the soybean precursor showed absorbance peaks at 292 and 301 nm. The peaks

characterized electron transition absorption $\pi - \pi^*$ the C=C bond in sp^2 -hybridized carbon and $n - \pi^*$ from the C=O and nitrogen-containing groups sp^3 carbon.³⁹ The addition of 5, 10, and 15% EDA as dopant agents shifted the wavelengths to the visible light regions at 340, 338, and 351 nm, respectively, which could be attributed to the presence of amine groups on the surface of CDs.⁴⁰ The amine groups act as an electron trapping site or trap for excited electrons, if more electrons are trapped, the light absorption also increases.⁴¹ The CDs with 15% EDA showed the highest absorption at 351 nm (near visible region <400 nm). The addition of dopants into CDs narrows the band gap energy in CDs, which minimizes the recombination of (e^-/h^+) pairs so that the CDs can exhibit wide light absorption. The formation of energy levels above the valence band (VB) trapping of the excited state is evidenced by the analysis of energy gap.

The energy gap value was calculated by the differential method of the first-order derivative of the absorbance (dA/dE), where dA was derivative absorbance and dE was the derivative energy gap.⁴² The calculation of E_g values was performed with the following eq 3.

$$E_g = \frac{1240}{\lambda \text{ (nm)}} \text{ eV} \quad (3)$$

The efficiency of electron–hole pair-induced separation was observable in the PL spectra as shown in Figure 2e. In general, there are three factors affecting the nature of PL properties of CDs, such as (1) energy gap (E_g), (2) the presence of functional groups in CDs structure, and (3) quantum particle size of the CDs.⁴³ Based on the fluorescence spectral characteristics, CDs from soybean showed peak fluorescence emissions at 468 and 492 nm (blue emission) excited by UV light at 395 nm wavelength. A strong emission in the visible beam region (>400 nm) could be attributed to the presence of heterogeneous groups in the structure of CDs.⁴⁴ Heteroatomic groups in CDs can be caused by the addition of dopant N from the EDA compound. N doping causes defects in the surface structure of CDs called surface passivation. This surface passivation process will produce a heteroatomic group that acts as an electron trap or acceptor from the excitation of the $\pi - \pi^*$ bond.⁴⁵ These results are consistent with the analysis results obtained from FTIR and UV–vis spectra on the formation of the C–NO₂ group (Figure 2a,b). The formation of C–NO₂ causes an increase in the wavelength of emissions and a decrease in the PL intensity, meaning that with the addition of dopant EDA, the electron–hole recombination process can be reduced so that the process of deprotonation or formation of h^+ increases.⁴⁶ In addition, CDs of 15% EDA have lower emission intensity than CDs of 5 and 10%. The lower PL emission intensity demonstrates a lower recombination rate of photogenerated (e^-/h^+) pairs.⁴⁷ Increased wavelength emissions and decreased emission intensity are useful aspects for the photocatalysis process.

The quantum yield (QY) of CDs was determined by comparing the optical properties of CDs to the standard quinine sulfate solution 0.54 M H₂SO₄ at an excitation wavelength of 350 nm. The QY of CDs samples was calculated by using the following eq 4.⁴⁸

$$QY_s = QY_r \times \frac{I_s}{I_r} \times \frac{OD_r}{OD_s} \times \frac{\eta_s^2}{\eta_r^2} \quad (4)$$

where S and R are the sample and reference (quinine sulfate), I is the PL area, OD is the absorbance value, and η is the refractive index of the solvent.

The QY of CDs and CDs samples with 5, 10, and 15% EDA was 28.31, 27.72, 25.17, and 21.03%, respectively, as shown in Table 2 and Figure 2d. QY decreased gradually with the

Table 2. Quantum Yield of CDs

materials	λ excitation (nm)	λ emission (nm)	QY (%)
CDs	395	465	28.31
CDs 5% EDA	395	491	27.72
CDs 10% EDA	395	491	25.17
CDs 15% EDA	395	492	21.03
Quinine sulfate	350	550	54

increasing fluorescence intensity. This is related to the photobleaching process, the induction of photons in diverse functional groups on the surface of the structure and changes in heteroatomic surface groups structural of CDs.⁴⁹

In Figure 2e, it can be seen that the increase of EDA concentration is directly proportional to fluorescent emissions and inversely proportional to the resulting QY. Changes in the structure of CDs are caused by the accumulation of “dot” particles called agglomerations. The addition of EDA dopants with high concentrations will cause agglomeration so that photon induction is disrupted, which results in a decrease in the QY value.

The morphological studies of the material and particle distribution of CDs 15% EDA sample were performed by using HR-TEM. Figure 3a indicates the shape and size of the CDs material (zero dimension). The calculation results from Figure 3d using Image J software showed that the average diameter of EDA-doped CDs particles at 15% concentration was 4.249 nm. Based on previous studies, the diameters of CDs from soybean flour and fermented soybean were 2.5 and 7 nm, respectively.^{50,56} These data have proved that soybean can become the precursor source for CDs with particle size distribution of below 10 nm.⁵¹ Figure 3b,c shows particle distribution and lattice distance of the CDs. By using Image J software, the lattice distance was found to be 0.4167 nm, which is ascribed to the distance between the carbon layers (002) of graphene. These results showed that CDs with 15% EDA dopant consisted of amorphous components and the crystals of carbon sp^2 graphite.^{52,53} Figure 3c also shows the uneven shape of dot particles; this result is in agreement with the QY analysis of 21.03%.

The phase analysis and material structure of the CDs were characterized using XRD. The CD diffractogram is shown in Figure 2f. A broad peak at $2\theta \sim 20^\circ$ corresponded to the carbon (002) hkl plane according to the JCPDS No. 26-1076 with an interlayer spacing of $d = 0.4175$ nm. This distance was higher than the standard graphitic carbon interlayer spacing, i.e., 0.33 nm.⁵⁴ This confirms that CDs are composed of a high amorphous composition. A broad peak at $2\theta = 20^\circ$ interplanar graphitic stacking plane of CDs and also indicated that CDs had a small particle size.^{55,56} This result was consistent with HR-TEM analysis, where the CDs had a particle size of below 5 nm and lattice distance 0.4167 nm.

The information about the condition of CD surface and chemical composition was analyzed in more detail through orbital transitions of each of the functional groups by using XPS. Figure 4a shows the XPS spectrum full survey scan that shows the presence of three components of CDs: C, O, and N. The three elements of CDs, such as C 1s, N 1s, and O 1s, have dominant peaks at 284.6, 399.6, and 534.1 eV, respectively. This

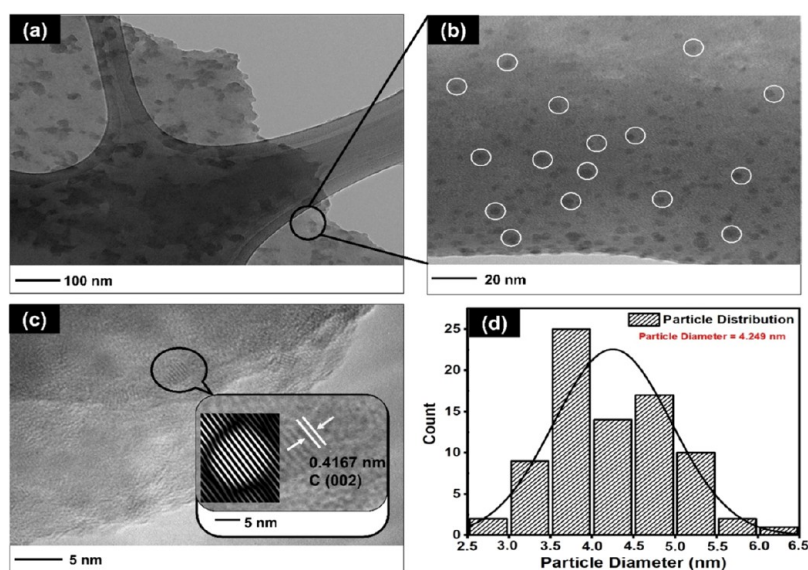


Figure 3. TEM images of CDs 15%EDA (a), HR-TEM images (b), lattice distance (c), and particle size distribution (d).

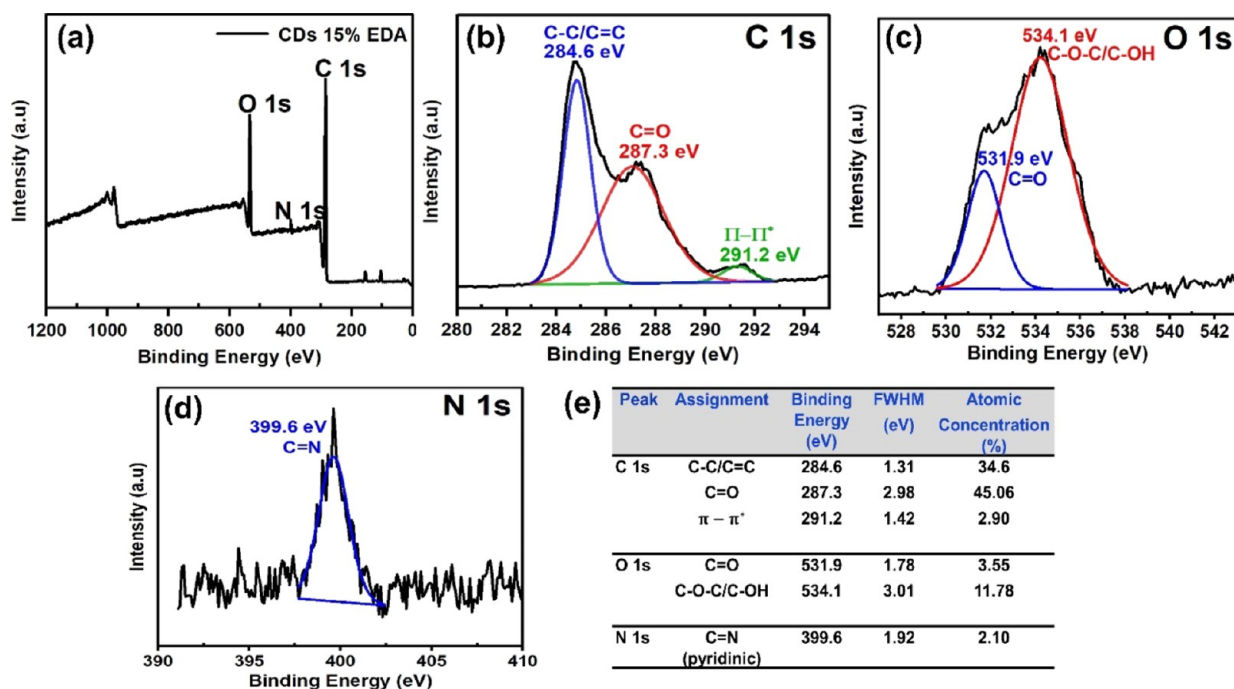


Figure 4. XPS spectrum of CDs 15% EDA (a), XPS high-resolution spectra of C 1s (b), O 1s (c), and N 1s (d), and summary of atomic concentration of each element (e).

information is summarized in Figure 4e. The C 1s spectra had three peak components showing C–C/C=C bonds at 284.6 eV for graphite and carbon sp^3 , C=O at 287.3 eV, which corresponded with the carbonyl groups, and the peak at 291.2 eV corresponded with the $\pi - \pi^*$ shake-up transitional process (Figure 4b).⁵⁷ The O 1s spectra had two peaks, such as at 531.9 eV as the C=O carbonyl bond and the highest intensity peak at 534.1 eV as the C–O–C/C–OH bond (Figure 4c).⁵⁸ The N 1s spectra had one pyridinic nitrogen peak, C=N, at 399.9 eV (Figure 4d).⁵⁹ These data have suggested that epoxide and hydroxyl groups were dominating the structure of CDs. Only a portion of N doping could be conjugated in the sp^2 orbital domain, which was about 2.10%. This analysis was consistent with the FTIR data showing low stretching vibrations N=C=

N at 2120 cm^{-1} wavenumber (Figure 2a) and diffraction peak at $2\theta \sim 20^\circ$ with a d-spacing of 0.4175 nm, which is the pyridinic N.

3.2. Characteristics of N-ZnO and N-ZnO/CD Nanocomposites. TGA was used to investigate the stability and weight loss of nanomaterials. In this study, TGA was used to determine the calcination temperature to obtain N-ZnO crystals. N-ZnO produced was later mixed with CDs 15% EDA to form N-ZnO/CD nanocomposites. Figure 5 shows the TGA thermogram of the N-ZnO material. The results showed that the initial mass reduction (−2.8 mg) occurred at 30–350 °C due to the desorption or material moisture removal process.⁶⁰ The second mass reduction (−1 mg) occurred at 350–600 °C, when most of the organic groups of urea compounds as N dopants in ZnO crystals underwent

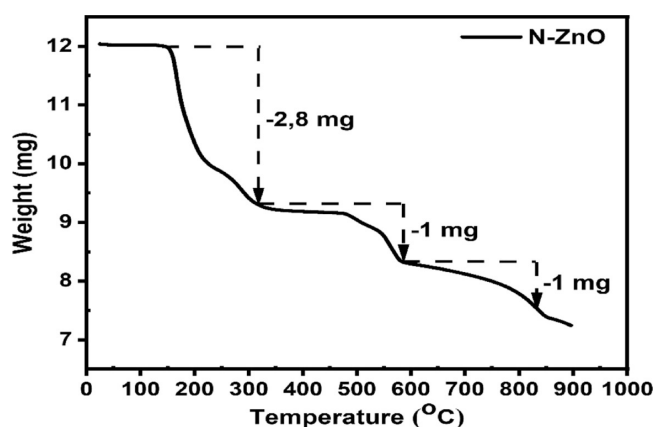


Figure 5. TGA spectrum of N-ZnO.

decomposition.⁶¹ The last mass reduction (−1 mg) occurred at 600–850 °C, in which the decrease was thought to be derived from the decomposition of ZnO.⁶² It can be concluded that a temperature of 600 °C indicates the presence of ZnO crystals. Based on the results of the TGA and some previous studies, the N-ZnO calcination temperature in this study was set at 500 °C for 2 h.

The XRD patterns of the samples are shown in Figure 6. As seen in Figure 6a, the XRD pattern of ZnO, N-ZnO nanoparticles, and N-ZnO/CD nanocomposites showed the strongest diffraction peaks at 2θ values of 31.8, 34.4, 36.2, 47.5, 56.6, 62.8, 66.4, 67.9, and 69.1° describing hkl planes of (100), (002), (101), (102), (110), (103), (200), (112), and (201), respectively. This diffraction pattern corresponded with the ZnO pure and standard of ZnO phase (JCPDS No. 36-1451), which is a hexagonal wurtzite of the polycrystalline structure.⁶³ The XRD pattern of N-doped ZnO and N-ZnO/CD nanocomposites showed no significant changes in characteristics of the ZnO phase. Liu and co-workers reported that heteroatomic doping does not affect the crystal structure and or any impurity nanomaterials. However, in some studies, doping atoms can cause angular shifts in diffraction patterns due to differences in the ionic radius.⁶⁴ He et al. studied the XRD pattern of Cu-doped BiVO₄, which showed a slight angular shift at $2\theta = 28.6$ – 29.2° compared to the undoped sample; the presence of

differences in ionic radius Cu^{2+} (0.072 nm) > V^{5+} (0.059 nm) caused the diffraction peaks to shift toward lower angles.⁶⁵

Based on the research of Atchudan et al. a broader weak diffraction peak at $2\theta = 19$ and 26° in Figure 6b is the peak of diffraction (002) of the carbon graphitic plane, which is common from carbon materials on the ZnO surface.²⁸ In this study, the presence of carbon material is indicated from the urea compound and CDs as a carbon amorphous on the ZnO surface. The average size and lattice distance of samples were calculated using the Debye–Scherrer equation and Bragg's Law (5) and (6), respectively.

$$D = \frac{K\lambda}{\beta \cos\theta} \quad (5)$$

$$n\lambda = 2d \sin\theta \quad (6)$$

where D is the crystallite size (nm), K is the Scherrer constant (0.9), λ is the wavelength of the incident X-rays ($\lambda = 0.15406$), β is the full width at half maximum (FWHM) of the diffraction peak, θ is the peak position, n is the order of diffraction, and d is the spacing between planes of given Miller indices h , k , and l .

The average crystallite size, the lattice parameter, and the cell volume of ZnO, N-ZnO nanoparticles, and N-ZnO/CD nanocomposites are reported in Table 3. The lattice parameter in the XRD plane direction is defined as the a -axis, and the c -axis is located in the out of plane. The hexagonal structure of ZnO pure has an average size value of 41.03 nm. In Figure 6c, there is no angular shift in the diffraction pattern of the samples. The ZnO diffraction peak based on (101) at $2\theta = 36.25^\circ$ has a lattice constant of 2.4759 nm with $a = b = 3.246$ Å and $c = 5.2004$ Å. In N-ZnO and N-ZnO/CDs, the average crystal size and lattice parameters are slightly lower than those of pure ZnO. The degree of distortion (R) ideal wurtzite structure = 1.⁶⁶ However, in this study, R samples decreased 0.87. These changes may be due to a decrease in the characteristic of the wurtzite structure (zinc blende meta-stable phases).^{67,68} Meta-stable ZnO phases cause the creation of distortion lattices by dopant in the ZnO lattice. Lattice distortion on the surface of the ZnO lattice will prohibit the growth of grains of ZnO, which is confirmed by the decrease in lattice parameters, unit cell volume, and the degree of distortion (Table 3).⁶⁹ Lattice distortion in the surface structure of ZnO will certainly change the optical behavior of N-

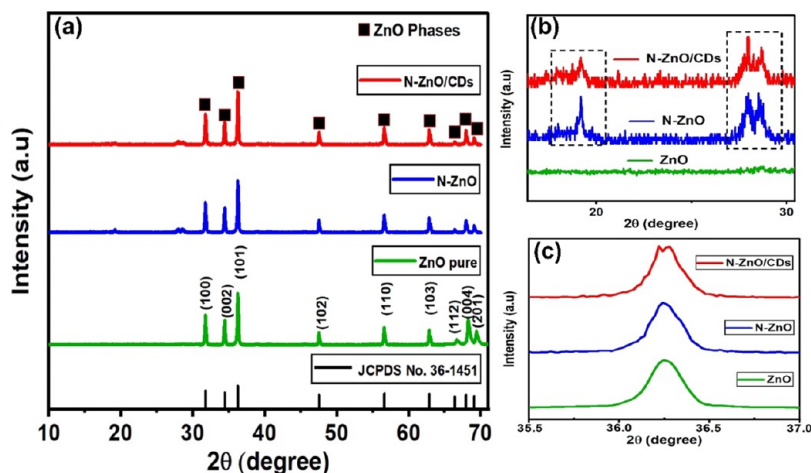


Figure 6. XRD patterns of ZnO, N-ZnO, and N-ZnO/CDs (a), XRD patterns of the samples in the 2θ value range of 15–30° (b), and XRD patterns of the samples peak (101) ZnO in the 2θ range = 35–37° (c).

Table 3. Cell Parameters and Crystallite of the Samples

sample	lattice parameter			unit cell volume (\AA^3)	average crystallite size (nm)	degree of distortion (R)
	$d_{(101)}$ (\AA)	$a = b$ (\AA)	c (\AA)			
ZnO pure	2.4759	3.2467	5.2004	47.473	41.03	1.01
N-ZnO	2.4576	2.7893	5.1987	25.338	35.21	0.87
N-ZnO/CDs	2.4575	2.7893	5.1987	25.338	38.47	0.87

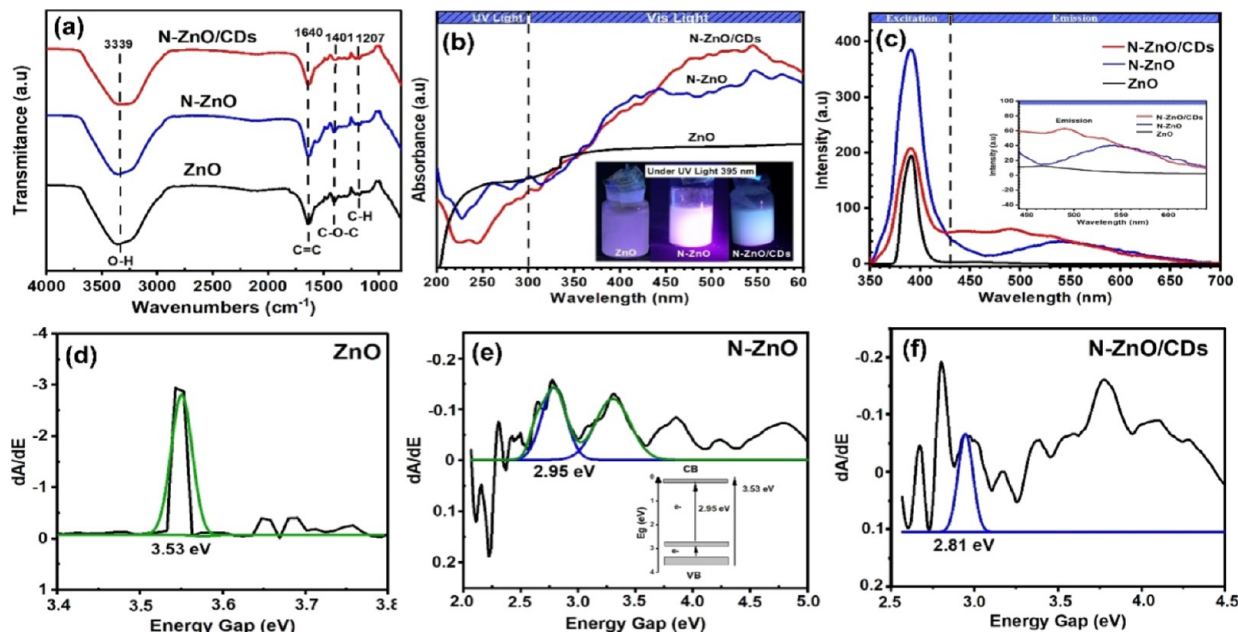


Figure 7. Analysis result characteristic of ZnO, N-ZnO, and N-ZnO/CDs. FTIR (a), UV–vis (b) (photograph fluorescents ZnO, N-ZnO, and N-ZnO/CD nanocomposites under UV lamp 365 nm courtesy of Dinda Gusti Ayu. Copyright 2022), photoluminescence (c), energy gap (d–f).

ZnO nanoparticles and N-ZnO/CD nanocomposites, which are certainly helpful for photocatalytic applications.

The FTIR spectrum of ZnO, N-ZnO nanoparticles, and N-ZnO/CD nanocomposites synthesized is shown in Figure 7a. The materials of pure ZnO, N-ZnO nanoparticles, and N-ZnO/CD nanocomposites had peak wavenumber values of 3339, 1640, 1401, and 1207 cm^{-1} ; their wavenumbers indicate the presence of O–H (stretching vibration), C=C (bending vibration), C–H (bending vibration), and C–O–C (bending vibration) groups, respectively.⁷⁰ There are no significant differences from the two spectra; however, at the peak of the wavenumber 1110 cm^{-1} it can be indicated as the peak of the C–O group in the N-ZnO nanoparticles and the epoxy group in N-ZnO/CD nanocomposites as well as at the peak of the wavenumber 998 cm^{-1} associated with the strain vibrations from Zn–O.⁷¹

The optical properties of ZnO, N-ZnO nanoparticles, and N-ZnO/CD nanocomposites were analyzed using UV–vis spectroscopy. The purpose of this analysis was to determine the absorbance ability and observe the changes in the band-gap energy (E_g) of the synthesized samples. Figure 7b shows that the material of ZnO has an absorbance peak characteristic at 350 nm in the UV light region and $E_g = \sim 3.50$ eV, indicating the presence of electron transition from the VB to the CB ($\text{O}_{2p} \rightarrow \text{Zn}_{3d}$).⁷² Based on XRD data analysis (Figure 6), there are two possibilities that occur in the heteroatomic doping process in the ZnO lattice, that is, lattice distortion and surface defect (Zn_{ni} or V_{O}).⁷³ In this study, dopant N was formed lattice distortion in the ZnO lattice. The formation of lattice distortion is indicated to be derived from the substitution of N^{3-} ions in the surface

structure of ZnO, because the ionic radii of N^{3-} (1.32 \AA) and O^{2-} (1.24 \AA) are very similar, which being the formation of vacancies is oxygen sites (V_{O}). Gupta et al. and Joshi et al. reported that the N atoms occupy the atomic interstitial sites of O atoms to the creation of V_{O} lead to an increase the absorption band in visible light regions and this conjugation has an effect of narrowing the band gap of ZnO.^{74,75}

The observation is in accordance with increased absorbance wavelengths of 420 nm (N-ZnO) and 441 nm (N-ZnO/CDs) (Figure 7b). In this study, dopant N in the ZnO lattice was formed oxygen vacancy. The oxygen vacancy (V_{O}) has most frequently invoked as an accidental source of n-type conductivity, but recent studies showed that this assignment cannot be correct. Although V_{O} has the lowest formation energy among some defects in ZnO, some studies report that V_{O} is the lowest donor and cannot contribute to n-type conductivity.^{76–81} Janotti and Chris studied that V_{O} is stable in the neutral charge state in n-type ZnO. V_{O} is a ‘negative- U ’ center, meaning that $\epsilon(2+/+)$ lies above $\epsilon(+/0)$ in the band gap. As the Fermi level moves upward, the charge transition is thus directly from the +2 to the neutral charge state.^{69,82} It should be noted that V_{O} cannot contribute to n-type conductivity in ZnO because it assumes the neutral charge state. Ni et al. reported that V_{O} is used for promoting the surface reaction because V_{O} can act as highly active sites by promoting the adsorption in the visible light regions.⁸³

Figure 7d–f shows that the samples had a decreased energy gap of 3.53 eV (ZnO), 2.95 eV (N-ZnO), and 2.81 eV (N-ZnO/CDs); it could also be related to the hybridization of N and O, which can be explained by the spin exchange interaction among

the band electrons and the localized electrons.⁸⁴ Sasinska et al. reported that N doping has two different possible spin configurations. The first one is paramagnetic with one unpaired electron which one lattice O^{2-} replaced by N^{2-} , i.e., ion N^{3-} with a localized hole above it. The second is diamagnetic with two unpaired electrons due to the replacement of one lattice O^{2-} by N^{3-} . That the N-doping substitution in the combination of V_O is modeled by substituting two neutrals of O atom with two N atoms and releasing one additional neutral O atom.⁸⁵ It means that removal of one neutral lattice oxygen atom has two extra unpaired. Lynch et al. reported the hybridization of less tightly bound N 2p levels with O 2p levels causing a reduction in band gap. The reduction of E_g is closely related to the Fermi level (E_f). Fermi energy complex has dependence on the type of defects and charge status (N^{3-} , Zn^{2+} , V_O).⁸⁶ However, further studies are needed to be able to explain the correlation between the VB and the defect of dopant N in the ZnO lattice.

The positions of band edges for the *n*-type semiconductor were estimated using the electronegativity concept to analyze the charge transfer mechanism of the N-ZnO/CD nanocomposites using eqs 7–9.

$$E_{CB} = \chi - E^\theta - 0.5E_g \quad (7)$$

$$E_{VB} = E_{CB} + E_g \quad (8)$$

$$\chi = [\chi(A)^a \chi(B)^b \chi(C)^c]^{1/(a+b+c)} \quad (9)$$

where E_g is the semiconductor band gap, E_{VB} and E_{CB} are the CB and VB edge potentials, respectively, E^θ represents the energy of free electrons on the hydrogen scale (4.5 eV) for the normal hydrogen electrode (NHE), χ (also known as Mulliken electronegativity) is the absolute electronegativity of the constituent atoms and *a*, *b*, and *c* are the number of atoms in the compound, while electronegativity of Zn and O was calculated as the arithmetic mean of the atomic electron affinity and the first ionization energy. Thus, $\chi_{Zn} = 4.5$ eV and $\chi_O = 7.54$ eV, so $\chi_{ZnO} = \sqrt{\chi_{Zn}\chi_O} = 5.79$ eV.⁸⁷ The measured bandgaps of ZnO, N-ZnO nanoparticles, and N-ZnO/CD nanocomposites were 3.53, 2.95, and 2.81 eV, respectively. The values of E_g , E_{CB} , and E_{VB} of ZnO, N-ZnO nanoparticles, and N-ZnO/CD nanocomposites (E_{CB} and E_{VB} are expressed in terms of NHE) are summarized in Table 4. Figure 8 shows the energy diagram of ZnO, N-ZnO nanoparticles, and N-ZnO/CD nanocomposites structure.

Table 4. Summary of the Values of the Bandgap (E_g), Conduction Band (E_{CB}), and Valence Band (E_{VB}) Edge Potentials

materials	E_g (eV)	E_{CB} (V)	E_{VB} (V)
ZnO	3.50	−0.475	3.055
N-ZnO	2.95	−0.185	2.765
N-ZnO/CDs	2.81	−0.115	2.695

The photoluminescence spectrum of ZnO, N-ZnO nanoparticles, and N-ZnO/CD nanocomposites in Figure 7c showed the presence of peak excitation at 390 nm and emission peak at 465, 537, and 550 nm, respectively. In this study, after the formation of V_O , there is a significant decrease in PL intensity of samples. Wang et al. reported that low PL intensity would result from the decreased radiative recombination, indicating that N-ZnO/CD nanocomposites showed high efficiency in separating

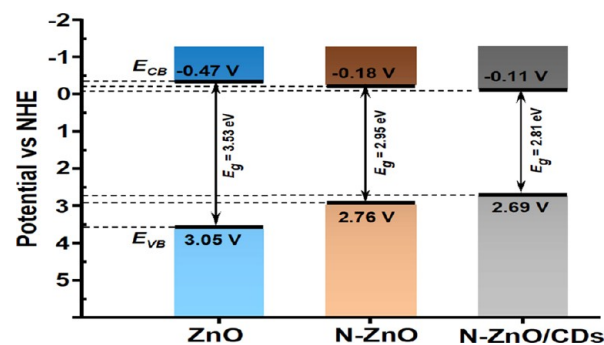


Figure 8. Bandgap structure of ZnO, N-ZnO, and N-ZnO/CD nanocomposites.

(e^-/h^+) pairs.⁸⁸ These results correlate with UV analysis (Figure 7b); the formation of V_O on the surface of the ZnO structure serves as an e^- charge carrier traps and thus assists to lower the recombination of (e^-/h^+) pairs.

In this study, we introduced CDs as supporting materials in N-ZnO photocatalysts. CDs are one of the green catalyst technologies that have been developed in various fields of research, because the source of precursors is eco-friendly (agricultural biomass) and can be synthesized via green methods. Agricultural biomass has functional groups such as phenolic, carboxyl, ketones, aldehydes, and alcohols. These organic functional groups have the potency to being photocatalyst materials in organic pollutant degradation via several mechanisms. As seen in Figure 7, the presence of CDs in N-ZnO/CD nanocomposites has an effect on increased absorbance in the UV light regions and also decreasing PL intensity. Based on analysis in Figure 2, CDs act as a multifunctional component in photocatalysts. There are several explanations about the function of CDs as supporting materials in the ZnO photocatalyst,

- CDs have absorbance near visible light region (351 nm) due to the presence of an electronic transition from the C=O or C=N bond, which can act to expand the absorption of photon energy in the visible beam region. So that photocatalytic activity was increased.⁸⁹
- CDs have hydroxyl, carboxyl, and amine functional groups on their surface. Das et al. studied these functional groups of CDs, such as −OH and −COOH can act as the active sites in the photocatalytic reaction from H-bonding interaction with organic pollutants.⁹⁰
- Quantum confinement effect: The small size of the CDs (4.249 nm), which allows energy bands to expand and create an increased CB. These will match with the energy band of ZnO and therefore the decreased intensity of PL N-ZnO/CDs.⁹¹

From several of the explanations above, it is known that the presence of CDs as a green technology catalyst will expand the photoresponse and increase ZnO photocatalytic activity.

The surface morphology of N-ZnO and N-ZnO/CDs investigated by FESEM analysis is shown in Figure 9. As seen in Figure 9, the N dopant and the addition of CDs had effect on the morphology of N-ZnO nanoparticles and N-ZnO/CD nanocomposites. The N-ZnO nanoparticles and N-ZnO/CDs nanocomposite showed rough hexagonal-like particle ZnO with an average diameter of 40 nm. The particle size is related to the variation of the crystallite size in Figure 6. The graphic of distribution particle size is shown in Figure 9a,c. The elemental

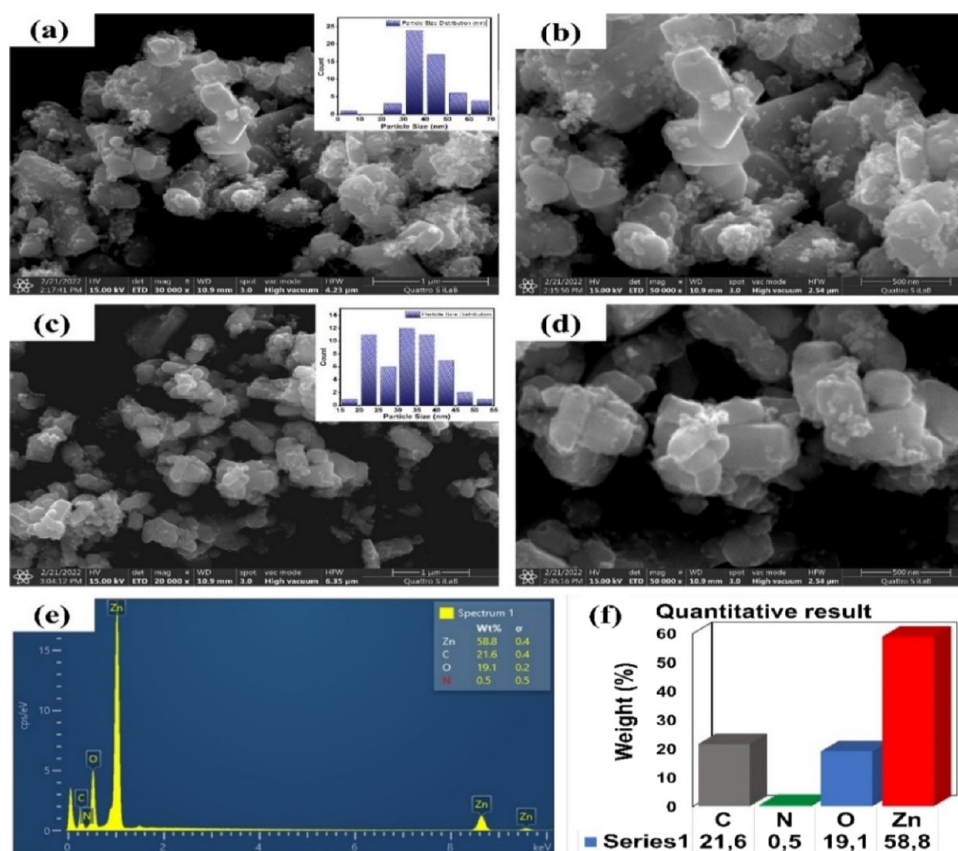


Figure 9. FESEM images of N-ZnO (inset (a) particle size distribution graph) (a, b), N-ZnO/CDs nanocomposite (inset (c) particle size distribution graph) (c, d), EDS spectrum of N-ZnO/CDs and quantitative result of presented elements in the N-ZnO/CDs nanocomposite (e, f).

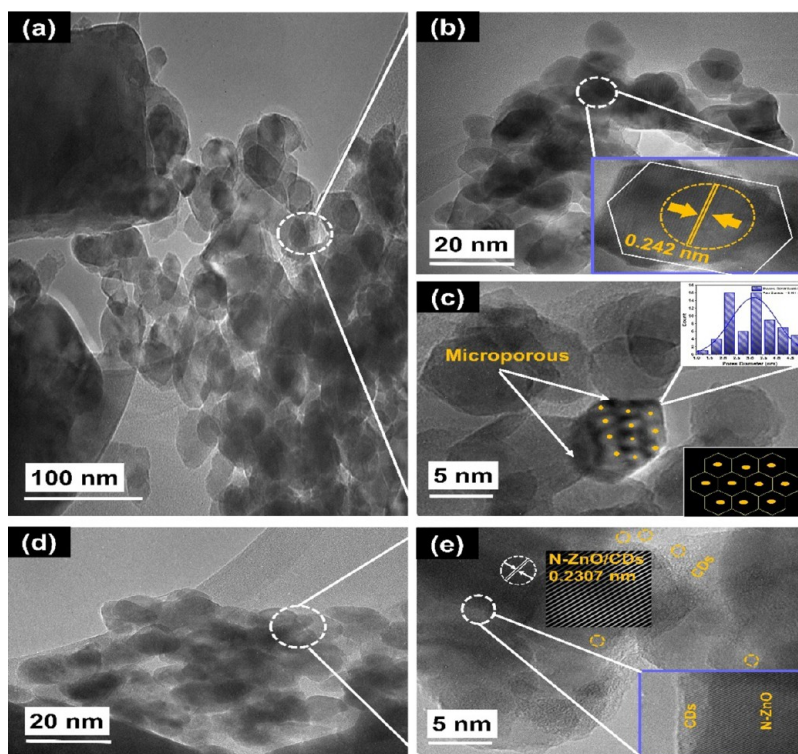


Figure 10. HR-TEM images of N-ZnO (inset (b, c) lattice distance and pore size graph) (a–c), and N-ZnO/CD nanocomposites and (inset (e)) values of lattice distance (d, e).

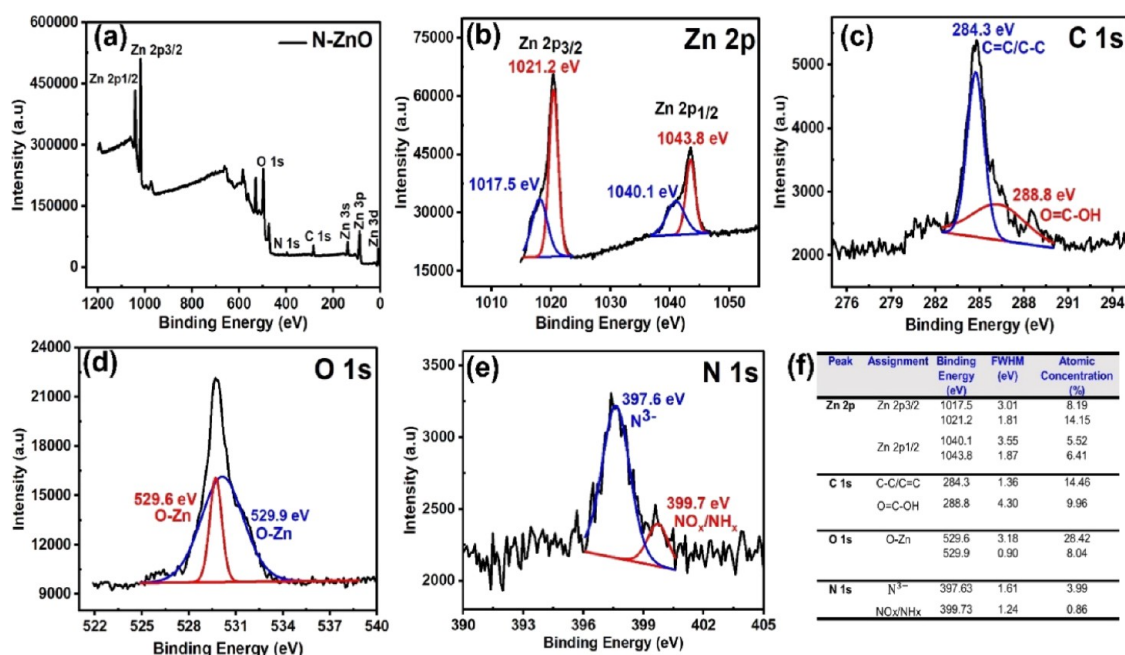


Figure 11. XPS full survey of N-ZnO (a), high-resolution XPS spectrum of Zn 2p (b), C 1s (c), O 1s (d), and N 1s (e), and summary of atomic concentration of each element (f).

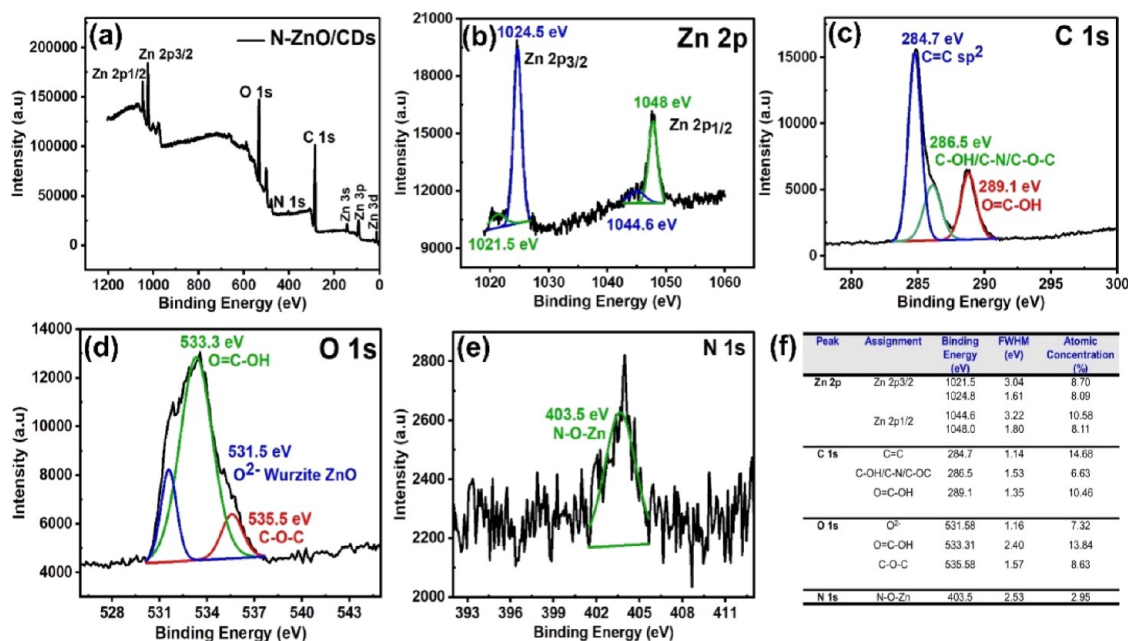


Figure 12. XPS full survey of N-ZnO/CDs (a), high-resolution XPS spectrum of Zn 2p (b), C 1s (c), O 1s (d), N 1s (e), and summary of atomic concentration of each element (f).

analysis of N-ZnO/CDs by the EDS spectrum is presented in Figure 9e and the quantitative result analysis shown in Figure 9f confirmed the presence of Zn (58.8%), O (19.1%), C (21.6%), and N (0.5%). The presence of the N element in N-ZnO/CD nanocomposites is 0.5%. These data showed that the dopant N and CDs have interacted on the surface of the ZnO structure, so that the creation rough formation on the surface of N-ZnO/CDs and the variety of particle size.

The internal morphology, particle size, crystal structure, and d-spacing of N-ZnO nanoparticles and N-ZnO/CD nanocomposites were investigated by HR-TEM analysis, and the representative morphology is shown in Figure 10. As seen in

Figure 10a N-ZnO has a variation in particle shape with varying particle sizes; this analysis correlates with the N-ZnO diffraction pattern (Figure 6) that N-ZnO has a meta-stable phase zinc blende structure. Jayanti et al. reported that oxygen vacancies will affect ZnO growth processes and nucleation, so this will affect their morphological changes.⁹² In Figure 10b, N-ZnO has a wurtzite hexagonal structure and a lattice distance of 0.242 nm, which confirmed *hkl* plane (101) of the ZnO crystal. In Figure 10c, the bright spot indicated corresponded to Vo in benzene hexagons of N-ZnO nanoparticles with average pores of 3.2 nm, which confirmed the microporous material.⁹³ The morphology of N-ZnO/CD nanocomposites is shown in Figure 10. Figure

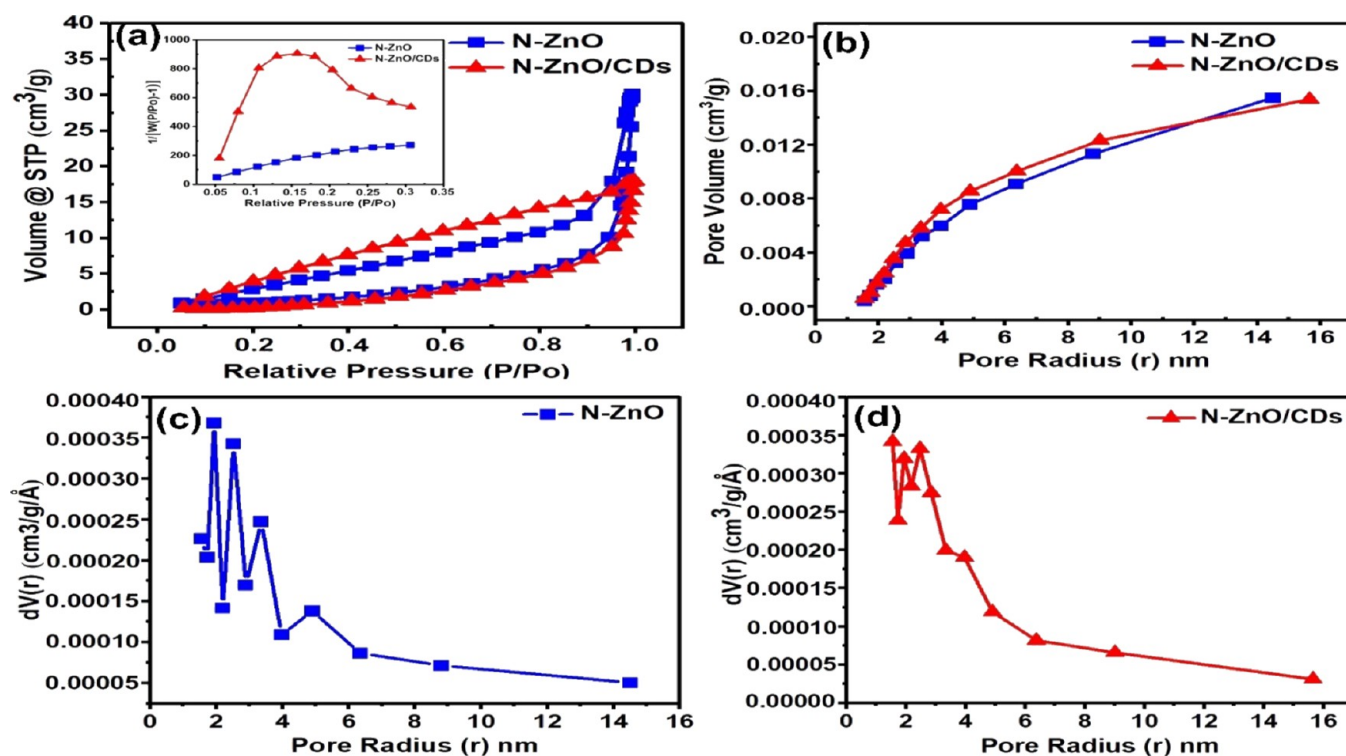


Figure 13. BET plot of the surface area of N-ZnO and N-ZnO/CD nanocomposites with the N₂ adsorption–desorption isotherm (inset specific desorption of the samples) (a), BET plot of distribution pore size of samples (b), and BJH plot of specific distribution pore size of N-ZnO and N-ZnO/CD nanocomposites (c, d).

10d shows that N-ZnO/CDs has slight particle shapes varied and lattice distance 0.2307 nm. There were no good pores in the N-ZnO/CD nanocomposites. The decrease of the lattice distance of N-ZnO/CDs in Figure 10e indicated derived from distribution CDs as decorated on the N-ZnO surface. Gao and Zhao and Long et al. reported that CDs have a small size particle and zero dimension, so that CDs have enough interface combining with N-ZnO nanoparticles.^{94,95} The morphology of CDs of N-ZnO was burger like.⁹⁶

The investigation of chemical state, surface chemical composition, and bonding environment N-ZnO and N-ZnO/CD nanocomposites used XPS analysis. The full survey XPS spectra of N-ZnO nanoparticles and N-ZnO/CDs nanocomposite shown in Figures 11a and 12a indicate the presence of Zinc (Zn 2p, Zn 3s, Zn 3p and Zn 3d), carbon (C 1s), oxygen (O 1s), and nitrogen (N 1s) in accordance with the chemical composition of the samples. Figures 11b and 12b show that the core-level high-resolution Zn 2p can be fitted with four peaks at 1017.5–1043.8 and 1021.5–1048 eV, respectively. The four peaks of Zn represented two orbitals of Zn 2p_{3/2} and Zn 2p_{1/2}. The Zn 2p spectra indicated the presence of Zn²⁺ ions in the tetrahedral structure of Zn–O bonds. The transitions of 2p_{3/2} to 2p_{1/2} were established based on the width of Lorentzian emission photo line.⁹⁷ The decreased intensity of Zn 2p_{1/2} and 2p_{3/2} indicated the presence of CDs on the surface of N-ZnO structure. Li et al. reported the decreased intensity which caused the change of bond structure between Zn and other atoms existed in N-ZnO/CD nanocomposites.⁹⁸ The C 1s spectra are shown in Figures 11c and 12c. There are two peaks at 284.3 and 288.8 eV which represented the C=C and O=C–OH (N-ZnO) and three peaks at 284.7, 286.5, and 289.1 eV which represented the C=C, C–OH, and O=C–OH (N-ZnO/CDs).⁹⁹ The spectrum C 1s had different atomic concentration

percent (Figures 11f and 12f), 24.42% (N-ZnO) and 31.77% (N-ZnO/CDs). The increase of carbon atoms in the nanocomposite indicates the CD distribution on the surface of N-ZnO structure. The O 1s spectra are shown in Figures 11d and 12d. The spectrum O 1s of N-ZnO showed two peaks at 529.6 and 529.9 eV, which represented O–Zn bonds from the ZnO wurtzite structure.¹⁰⁰ The spectrum of the N-ZnO/CDs nanocomposite showed three peaks at 531.4, 532.9, and 535.9 eV, which represented O^{2−} ions Zn–O bond and oxygen-containing groups (C–OH, O=C–OH, C–O–C) on the surface of the ZnO structure. The shifted peak O^{2−} at 529.6 eV (N-ZnO) and 531.4 eV (N-ZnO/CDs) implied the presence of electronic interaction between ZnO and CDs.⁹⁸ The N 1s spectra are shown in Figures 11e and 12e. The N-ZnO presents two peaks N 1s at 397.6 (N^{3−}) associated with metallic nitrites (N–Zn bindings) and 399.7 eV (NO_x or NH_x) associated with nitrogen molecules bound and adsorbed on the surface of N-ZnO.^{101,102} Several reports studied the presence of the peak in 397–398 eV range, implying substitutional nitrogen doping O–Zn–N (N_{subst}) and other peaks at 399–400 eV indicating the presence of oxidized nitrogen species such as NO_x, NH_x, or NHOH.^{103,101} The N-ZnO/CD nanocomposites present one peak N 1s at 403.5 eV, which confirmed the interstitial nitrogen doping N–O–Zn (N_{inters}). The peak N–Zn–O bond at 397.6 eV with the atomic concentration (3.99%), which can cause nitrogen atoms to adsorb on the surface of the oxide on the surface structure ZnO.¹⁰⁴ The chemical state of Zn could indirectly reflect the bonding state of N and the relative quantity of Zn–N.¹⁰⁵

Chiesa et al. confirmed about substitutional nitrogen doped on ZnO polycrystalline that if the O^{2−} oxide anion is replaced by a N^{2−}, the overall charge balance does not change, thus in the solid physics trade defect is termed N⁰.¹⁰⁶ This studied

correlates with XRD analysis in Table 3, where the dopant N created the formation V_O when the N takes the place of O in the lattice of the ZnO, but not change structure wurtzite, as seen a slight in the decreased lattice peak hkl (101) at $2\theta = 36.25^\circ$ of ZnO. The decreased c-axis lattice constant 5.1987 Å, which is that Zn-N has a shorter bond-length than Zn–O, but the difference is relatively small, because the dopant N will randomly distribute in the lattice of ZnO and caused additional collapse of Zn tetrahedrons around oxygen sites.¹⁰⁷ From this investigation, it can be concluded that the presence of two peaks N 1s indicated the substitutional nitrogen state and the interstitial nitrogen state, which is described as N_O .

The specific surface area (S_{BET}) was analyzed by using the BET, and pore volume and pore size distribution were fitted with BJH methods of N_2 gas isotherm at 77 K as shown in Figure 13 and Table 5. Figure 13a shows the N_2 adsorption–desorption

Table 5. BET Surface Analysis and pore Distribution of N-ZnO and N-ZnO/CD Nanocomposites

materials	S_{BET} ($m^2 g^{-1}$)	pore volume ($cm^3 g^{-1}$)	average pore width (nm)	BJH pore adsorption (nm)	BJH surface area ($m^2 g^{-1}$)
N-ZnO	3.827	0.0459	24.0	1.939	8.320
N-ZnO/CDs	3.757	0.0277	14.78	1.550	8.152

isotherms of N-ZnO nanoparticles and N-ZnO/CD nanocomposites, where the graph is classified as a type IV adsorption isotherm according to the IUPAC classification.¹⁰⁸ The BET surface area of N-ZnO nanoparticles and N-ZnO/CD nanocomposites was found to be 3.827 and 3.757 $m^2 g^{-1}$, respectively. The BJH method graph in Figure 13b showed the pore volume distribution of N-ZnO and N-ZnO/CD nanocomposites, which are present at low P/Po (0–0.05) and

volume pores of N-ZnO nanoparticles (Figure 13c) and N-ZnO/CD nanocomposites (Figure 13d) were found to be 0.0459 $cm^3 g^{-1}$ at radius 1.939 nm and 0.0277 $cm^3 g^{-1}$ at radius 1.550 nm, respectively. These materials are classified as microporous-like materials, which is confirmed by the plateau and a H3 hysteresis loop.¹⁰⁹ The decrease in S_{BET} and pore volume adsorption of the samples indicated the collapse of the pores and agglomeration. The presence of CDs on the surface of N-ZnO nanoparticle structure can cause agglomeration. The amorphous carbon of the CDs agglomerated on the surface of the ZnO crystal so that it created the surface morphology as a burger like.

3.3. Photocatalytic Degradation Study. The photocatalytic activity of CDs, N-ZnO nanoparticles, and N-ZnO/CD nanocomposites was tested. These were used to study the photo decolorization of methylene blue (10 ppm) in aqueous solution under UV-B light irradiation at room temperature. The inset of Figure 14a shows percent decolorization of MB which is present in the following sequence, N-ZnO/CDs (83.4%) > N-ZnO (70.3%) > CDs (9.48%). These results were obtained from the calculation of the absorbance peak intensity of MB centered at 670 nm after irradiation process in Figure 14b. The decreased absorbance intensity peak and concentration of MB (Figure 14c) indicated that MB is degrading. By the pseudo first-order kinetic eq 10 fitting in Figure 14d, the photocatalytic rate constant (k) of MB degradation using N-ZnO/CD nanocomposites was calculated as 0.0299 min^{-1} , while for N-ZnO, it was 0.0202 min^{-1} and CDs 0.0016 min^{-1} .

The kinetics of MB decolorization with all produced photocatalysts was calculated used pseudo first-order kinetic in eq 10.

$$\ln(C_0/C_t) = kt \quad (10)$$

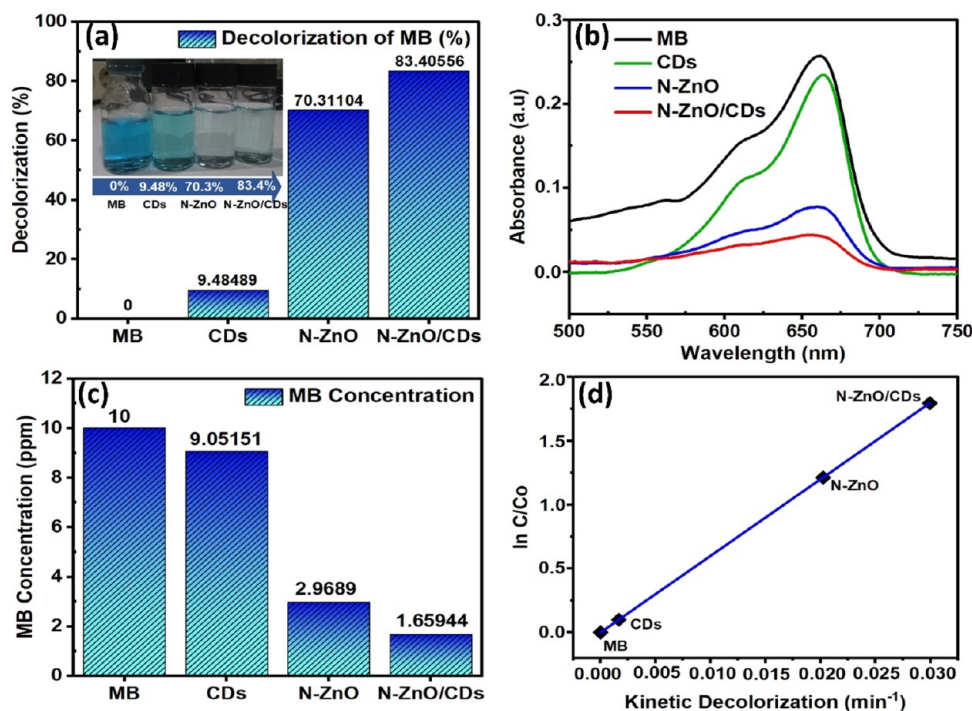


Figure 14. Decolorization percentage of MB (a) (photograph of decolorization of MB with different photocatalyst, courtesy of Dinda Gusti Ayu. Copyright 2022), absorbance peak of MB centered at 670 nm and MB concentration before and after irradiation with different photocatalyst (b, c), decolorization kinetics according to pseudo-first-order kinetics for different photocatalysts (d).

where C_0 and C_t are the concentration of MB before and after irradiation, t is irradiation time, and k is the pseudo first-order rate constant.

The mechanism of photocatalytic degradation of MB with N-ZnO/CDs under UV-B light irradiation is shown in Figure 15. In

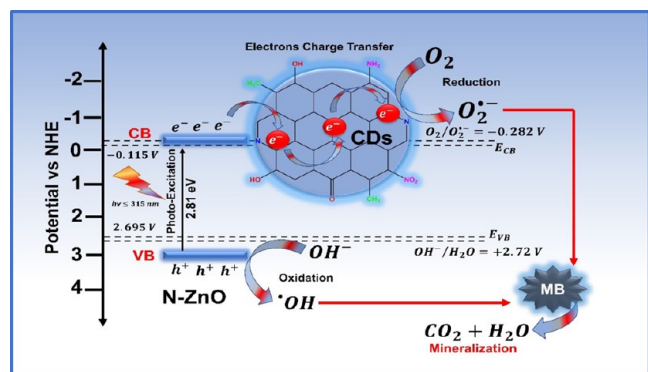
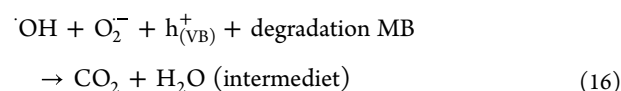
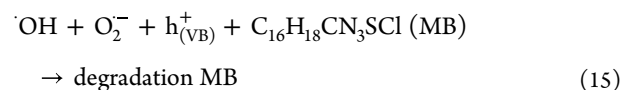
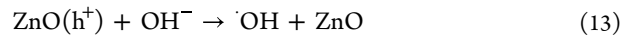
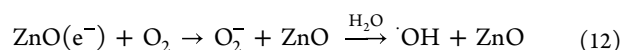
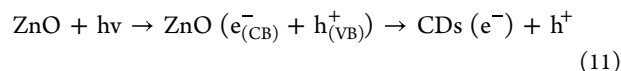


Figure 15. Mechanism of the charge electrons transfer in the photocatalytic degradation of N-ZnO/CD nanocomposites.

the photodegradation process under UV-B light irradiation, the photon energy from the UV-B lamp will be absorbed by N-ZnO/CD nanocomposites, the excitation from the N_O to CB of ZnO. Then the electron can be trapped by the oxygen vacancy, which is an energetically favorable process, to suppress recombination (e^-/h^+) pairs which will increase photocatalytic activity. The excitation process created holes (h^+) in the valence band and electrons (e^-) in the conduction band (CB). The reduction reaction process is where electrons will react with H_2O to form a radical O_2^- and $\cdot OH$. The oxidation process reaction where h^+ will react with H_2O to form a radical species $\cdot OH$. These radicals play a role in breaking down MB aromatic bonds into harmless compounds such as CO_2 , H_2O , and other mineral compounds. As mentioned in XPS analysis above, dopant N on the surface N-ZnO created formation of the N_O . These is due to the excitation of the N-ZnO band gap which transfer the e^- photogeneration of VB which is made of N_O orbitals to CB of the Zn 2p orbital, resulting in an increased electron density around Zn. Meanwhile, photogenerated h^+ is temporally stored in the VB. Then the electron can be trapped by the oxygen vacancy, which is an energetically favorable process. Ni et al. reported V_O as a mediator to facilitate the separation of (e^-/h^+) carriers, and additional V_O surface N-ZnO/CDs will act as highly active sites to promote the adsorption and activation of H_2O/OH^- . After photoexcitation, V_O can serve as an electron reservoir to store photogenerated electrons, so only a portion of the photoelectrons are transferred to the CB. Accordingly, the photocurrent gradually increases which occurs to capture and store photoexcited electrons, so V_O

can suppress the (e^-/h^+) recombination and thus improve photocatalytic activity.¹¹⁰

The photocatalytic efficiency was improved with the adding CDs as act supporting materials of N-ZnO/CD nanocomposites. The photogenerated electrons could be transferred to adsorbed CDs on the surface of ZnO where they were susceptible to react with the adsorbed oxygen molecules (O_2) to generate oxygen-reactive radicals (O_2^-). In this study, the optical energy gap is lower (2.81 eV). Li et al. studied the structure of the pyridine ring on the edge of graphitic carbon nitride (CN) framework, and CN was used to promote charge separation.¹¹¹ Roza et al. reported CDs on the surface of N-ZnO have electronic transitions of the $n - \pi^*$ from $C=O$ and $C=N=C$ and $\pi - \pi^*$ from $C=C$ (sp^2) so that to reduce the recombination (e^-/h^+) pairs on the surface of N-ZnO.¹¹² The efficient charge transfer for photoreaction between N-ZnO with CDs and created high density of separated h^+ to support the formation of active radicals, which contribute to degradation of MB. In addition, some reports indicated that the functionality groups are on the edge of CDs, such as C-OH can effectively promote separation charge carriers due to directional electron transfer.¹¹³ The reaction steps of photocatalytic degradation of MB were summarized (eqs 11–16). As shown in Table 6, the CDs can enhance the optical and photocatalytic activity of ZnO for pollutant degradation.



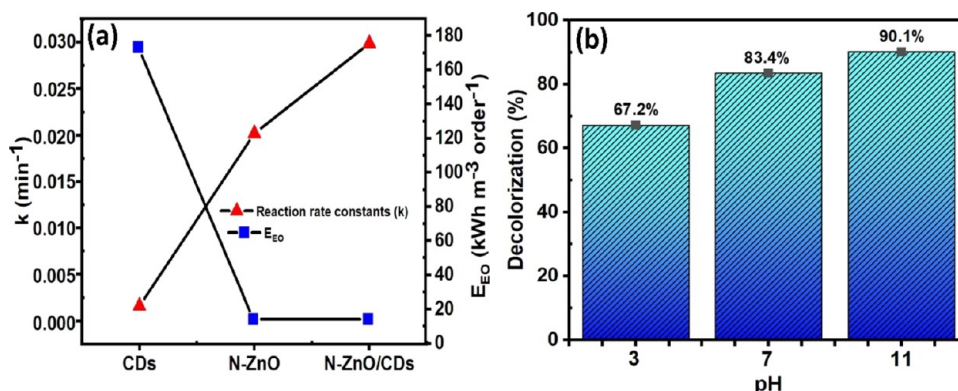
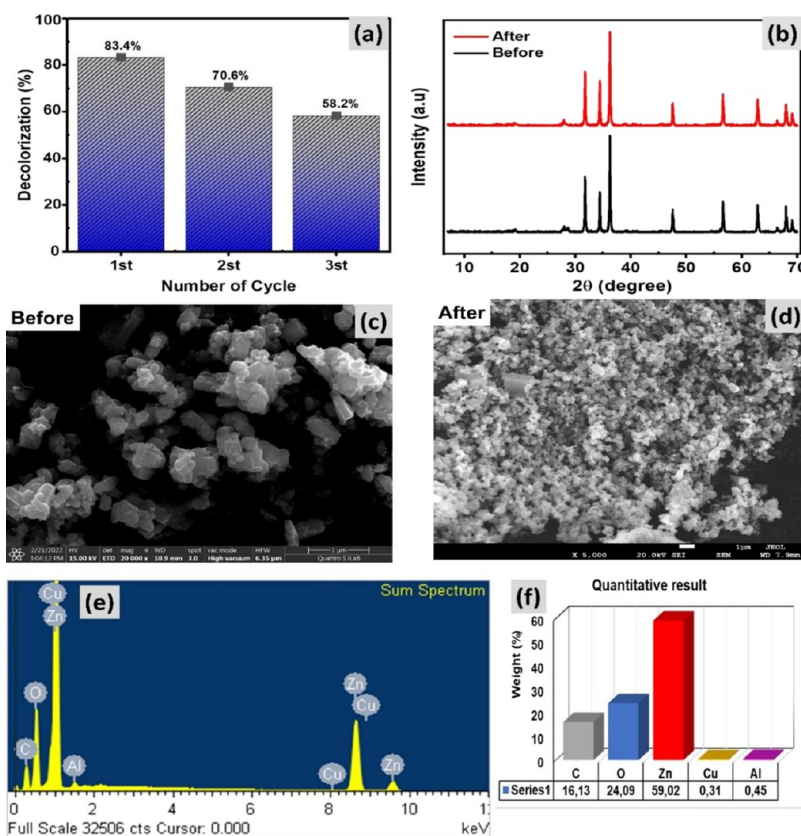
The value of χ of ZnO was calculated to be 5.79 eV, while N-ZnO/CD nanocomposites have E_{CB} and E_{VB} , which were estimated to be -0.115 and 2.695 V versus NHE. The conduction band of N-ZnO/CD nanocomposites was more enough positive than that the redox potential of O_2/O_2^- (-0.282 eV vs NHE) to react with O_2 to generate radical superoxide anions O_2^- , which might further react directly with the MB to give degradation products. The valence band of N-ZnO/CDs (2.695 V vs NHE) was positive to oxidize the potential redox OH^-/H_2O (2.72 V vs NHE) to form active radical hydroxyl

Table 6. Several Studies of Photocatalytic Activity in Degrading Organic Pollutants

photocatalyst	band gap (eV)	pollutant	light source	irradiation time (min)	degradation (%)	references
N-ZnO/C-dots	2.75	MG	visible Philips bulb (150 W)	100	70	114
ZnO/C-dots	3.23	MB	UV lamp (20 W)	70	74.98	112
NPQD/ZnO	3.13	MB	daylight xenon lamp (300 W)	30	90	115
N-GQDs/ZnO	2.65	MB	mercury lamp	120	100	116
this study	2.81	MB	UVB lamp (75 W)	60	83.4	

Table 7. Pseudo-First-Order Rate Constant for Decolorization of MB (mg L^{-1}) by UV-B Light (75 W m^{-2}) in the Presence of Various Photocatalyst Materials

material	decolorization (%)	MB concentration (ppm)	$\ln(C/C_0)$	k (min^{-1})	E_{EO} ($\text{kWh min}^{-3} \text{ order}^{-1}$)
CDs	9.48	9.05	0.0996	0.0016	173.29
N-ZnO	70.3	2.96	1.2144	0.0202	14.22
N-ZnO/CDs	83.4	1.65	1.7961	0.0299	14.22

**Figure 16.** Electrical energy consumption values ($\text{kWh min}^{-3} \text{ order}^{-1}$) and reaction rate constant (min^{-1}) (a) and the photocatalytic activity of N-ZnO/CDs photocatalyst at pH 3, 7, and 11 (b).**Figure 17.** Photostability graph for decolorization of MB at tree cycling runs over N-ZnO/CD nanocomposites (a), XRD diffractogram, FESEM images, EDX analysis and quantitative result element weight percent of N-ZnO/CD nanocomposites before and after tree cycling of the photolysis experiments (b–f).

$\cdot\text{OH}$. These results demonstrated that the active radicals $\cdot\text{OH}$ were mainly to the degradation of MB.

The UV process is one of the most effective methods for activation of photocatalytic degradation of organic compounds and the process is carried out to intensively demand electrical energy. In this study, we tried to find the relationship between

electrical energy E_{el} (kWh min^{-1}), and the overall reaction kinetics of advanced oxidation processes (AOPs). AOPs are defined as the electrical energy required to remove of MB. Bolton et al. introduced the figure-of-merit “electrical energy per order” (E_{EO}) to use in the first order-kinetic regime of AOPs and it is defined as the number of kWh electrical energy needed to

eliminate the concentration pollutant in 1 m³ of contaminated water by one order magnitude, the E_{EO} values can be calculated using eq 17.¹¹⁷

$$E_{EO} = \frac{Pt \times 1000}{V \times \log(C_0/C_t)} \quad (17)$$

where P is the power of UV lamp (kW), t is the irradiation time (min), V is the volume (L) of the water inside the reactor, C_0 and C_t are the initial and final pollutant concentrations, respectively. The efficiency of UV process was examined by the decolorization of the solution containing an MB. The values of E_{EO} for different photocatalysts is shown in Table 7. Pseudo-first-order rate constant for decolorization of MB (mg L⁻¹) by UV-B light (75 W m⁻²) in the presence of various photocatalyst materials.

Figure 16a shows that the values of E_{EO} decreased with increased decolorization and reaction kinetics. This result can be explained that the performance of the photocatalyst material in UV light absorbed is the main parameter affecting the decolorization of MB, because the mechanism of dye decolorization in UV-B light irradiation is based on the formation of radical produced by the photogenerated e⁻ in the photocatalyst material. The rate of photogenerated e⁻ increased with decreased energy gap of N-ZnO/CD nanocomposites, and then recombination (e⁻/h⁺) pairs can be suppressed, so that high free radicals can be produced and the rate of the photodegradation process of MB can be increased.

The pH of the solution has a key role in the photocatalytic reaction because the waste water from the textile industry consists of several pH so necessary to diagnose the effect of pH on decolorization of MB under UV-B light irradiation for 60 min. The pH of MB solution was adjusted using a 0.02 N sulfuric acid (pH = 3), and sodium hydroxide (pH = 11). In this study, the influence of solution pH for decolorization of MB was examined and is presented in Figure 16b.

Photocatalyst N-ZnO/CD nanocomposites showed decolorization of MB in basic condition (90.1%), neutral pH (83.4%) and acid pH (67.2%). At acid condition showed the low degradation of MB, this indicated with corrosion of the photocatalyst. Figure 16b shows that a neutral and basic pH has better efficiency. pH 11 shows higher decolorization with a degradation efficiency of 90.1%. The higher decolorization at basic pH is related to the interaction between cationic MB molecules and negatively charged surface of the N-ZnO/CD nanocomposites and created environment, which causes more pollutant ion adsorption.¹¹⁸ Photocatalysts negatively charged through ions (OH⁻) will form a lot of hydroxyl radicals, so there is an increase of photolysis reaction.¹¹⁹

3.4. Reusability of the Photocatalyst. The recyclability of photocatalyst N-ZnO/CDs was evaluated by the decolorization experiment for three reaction cycles shown in Figure 17. Figure 17a shows that after each reaction cycle, the photocatalyst of N-ZnO/CD nanocomposites was collected by centrifugation at 5500 rpm for 10 min, washed five times with ethanol, and dried in an oven at 70 °C for 2 h for the next photocatalytic degradation experiment. As a result, the photocatalytic efficiency of N-ZnO/CD nanocomposites in neutral pH (pH = 7.04) decreased from 83.4% (cycle 1), 70.6% (cycle 2), and 58.2% (cycle 3). Figure 17b shows the XRD diffractogram before and after three-cycle photocatalytic degradation of MB, which revealed no difference in the crystal structure of N-ZnO/CD nanocomposites. Figure 17c,d shows FESEM images before and after three-cycle photocatalytic degradation of MB. The

morphology of N-ZnO/CD nanocomposites remained unchanged in terms of particle shape after experiment. Figure 17e,f shows the EDS spectrum and quantitative result of N-ZnO/CD nanocomposites after three-cycle photocatalytic degradation of MB, the low decreased weight percent in carbon and nitrogen element (compared to Figure 17f). Zhang et al. reported the decreased of N-ZnO/CD nanocomposites for degradation efficiency which indicated a decrease in the content of CDs on the surface of N-ZnO structure after tree reaction cycle.¹²⁰ The result showed that CDs can effectively inhibit the photo-corrosion of N-ZnO. The result revealed that N-ZnO/CD nanocomposites as photocatalyst have good stability for the next recycle reaction photocatalytic degradation of other organic pollutants.

4. CONCLUSIONS

In conclusion, the photocatalyst materials of CDs, N-ZnO nanoparticles, and N-ZnO/CD nanocomposites were successfully synthesized by a simple hydrothermal methods and calcination process. The absorption spectra of CDs (351 nm), N-ZnO (420 nm), and N-ZnO/CDs (441 nm) were observed in the near to visible region with values of E_g 3.53, 2.95, and 2.81 eV, respectively. The N-ZnO and N-ZnO/CDs exhibited a wurtzite structure by using XRD characterization. The degree of distortion ($R = 0.87$) which indicated zinc blende meta-stable phases and its average particle size was determined as 35.21 and 38.47 nm, this result is correlated with FESEM analysis. The successful formation of N-ZnO and N-ZnO/CDs was confirmed by XPS analysis. These verified that the peak N 1s at 397.6 and 403.5 eV revealed dopant N on the surface of ZnO created N substitutional (N–Zn–O) and N interstitial (N–O–Zn) with the low atomic concentration < 5%. The S_{BET} and BJH pore distribution analyses showed that N-ZnO and N-ZnO/CDs belonged to the microporous catalyst with a H3 hysteresis loop and classified type IV isotherms according to the IUPAC. The performance of photocatalyst CDs, N-ZnO nanoparticles, and N-ZnO/CD nanocomposites was tested for decolorization of MB. The N-ZnO/CD nanocomposites showed high activity (83.4%, in 60 min); this result verified that the CDs can act as a supporting material for increased photodegradation activity. The N-ZnO/CD nanocomposites were also reused with a percentage degradation of MB (58.2%) after three-cycle experiments. The FESEM EDS and XRD analysis also showed that the N-ZnO/CD nanocomposites as a photocatalyst have good stability for further degradation studies.

AUTHOR INFORMATION

Corresponding Author

Saharman Gea – Department of Chemistry, Faculty of Mathematics and Natural Sciences and Cellulosic and Functional Materials Research Centre, Universitas Sumatera Utara, Medan 20155, Indonesia; orcid.org/0000-0003-0615-0918; Email: s.gea@usu.ac.id

Authors

Dinda Gusti Ayu – Postgraduate School, Department of Chemistry, Faculty of Mathematics and Natural Sciences, Department of Chemistry, Faculty of Mathematics and Natural Sciences, and Cellulosic and Functional Materials Research Centre, Universitas Sumatera Utara, Medan 20155, Indonesia

Andriyani — Department of Chemistry, Faculty of Mathematics and Natural Sciences, Universitas Sumatera Utara, Medan 20155, Indonesia

Dewi Junita Telaumbanua — Department of Chemistry, Faculty of Mathematics and Natural Sciences, Universitas Sumatera Utara, Medan 20155, Indonesia

Averroes Fazlur Rahman Piliang — Cellulosic and Functional Materials Research Centre and Department of Physics, Faculty of Mathematics and Natural Sciences, Universitas Sumatera Utara, Medan 20155, Indonesia

Mahyuni Harahap — Department of Chemistry, Faculty of Science Technology and Information, Universitas Sari Mutiara Indonesia, Medan 20124, Indonesia

Zhihao Yen — School of Materials Science and Engineering, Nanyang Technological University, Singapore 639798, Singapore

Ronn Goei — School of Materials Science and Engineering, Nanyang Technological University, Singapore 639798, Singapore; orcid.org/0000-0001-6794-0601

Alfred Iing Yoong Tok — School of Materials Science and Engineering, Nanyang Technological University, Singapore 639798, Singapore; orcid.org/0000-0003-3546-7180

Complete contact information is available at:

<https://pubs.acs.org/10.1021/acsomega.2c07546>

Notes

The authors declare no competing financial interest.

ACKNOWLEDGMENTS

The authors are grateful for the financial support from KEMENRISTEK DIKTI, Republic Indonesia, DRPM-PTM 2022 program with contract number of 097/E5/PG.02.00.PT/2022 and thankful for the School of Materials Science and Engineering, Nanyang Technological University (NTU), Singapore, for help to conducting the XPS and HR-TEM analysis of the photocatalyst materials in this study.

REFERENCES

- (1) Bandekar, G.; Rajurkar, N. S.; Mulla, I. S.; Mulik, U. P.; Amalnerkar, D. P.; Adhyapak, P. V. Synthesis, Characterization and Photocatalytic Activity of PVP Stabilized ZnO and Modified ZnO Nanostructures. *Appl. Nanosci.* **2014**, *4*, 199.
- (2) Shao, Y.; Wang, X.; Kang, Y.; Shu, Y.; Sun, Q.; Li, L. Application of Mn/MCM-41 as an Adsorbent to Remove Methyl Blue from Aqueous Solution. *J. Colloid Interface Sci.* **2014**, *429*, 25.
- (3) Phillips, K. A.; Yau, A.; Favela, K. A.; Isaacs, K. K.; McEachran, A.; Grulke, C.; Richard, A. M.; Williams, A. J.; Sobus, J. R.; Thomas, R. S.; Wambaugh, J. F. Suspect Screening Analysis of Chemicals in Consumer Products. *Environ. Sci. Technol.* **2018**, *52*, 3125–3135.
- (4) Iqbal, M. Vicia Faba Bioassay for Environmental Toxicity Monitoring: A Review. *Chemosphere* **2016**, *144*, 785.
- (5) Senthil Kumar, M.; Arunagiri, C. Efficient Photocatalytic Degradation of Organic Dyes Using Fe-Doped ZnO Nanoparticles. *J. Mater. Sci.: Mater. Electron.* **2021**, *32*, 17925–17935.
- (6) Citronnelle, C. C.; Toufaily, J.; Hamieh, T. Biosorption Of Methylene Blue From Waste Water Using Lebanese Akram Hijazi. *Eur. Sci. J.* **2015**, *11*, 293–308.
- (7) Almasoud, N.; Wabaidur, S. M.; Allothman, Z. A.; Ghfar, A. A.; Alomar, T. S. A Solid Phase Extraction Based Uplc-Esi-MS/MS Method Using Surfactant-Modified Clay as Extraction Sorbent for the Removal Andetermination of Rhodamine b in Industrial Wastewater Samples. *Desalin. Water Treat.* **2020**, *195*, 222.
- (8) Faryadi, M.; Rahimi, M.; Akbari, M. Process Modeling and Optimization of Rhodamine B Dye Ozonation in a Novel Microreactor Equipped with High Frequency Ultrasound Wave. *Korean J. Chem. Eng.* **2016**, *33*, 922.
- (9) Shakir, K.; Elkafrawy, A. F.; Ghoneimy, H. F.; Elrab Beheir, S. G.; Refaat, M. Removal of Rhodamine B (a Basic Dye) and Thoron (an Acidic Dye) from Dilute Aqueous Solutions and Wastewater Simulants by Ion Flotation. *Water Res.* **2010**, *44*, 1449.
- (10) Hou, M. F.; Liao, L.; Zhang, W.; Tang, X. Y.; Wan, H. F.; Yin, G. C. Degradation of Rhodamine B by Fe(0)-Based Fenton Process with H₂O₂. *Chemosphere* **2011**, *83*, 1279.
- (11) Ahmad, M.; Ahmed, E.; Hong, Z. L.; Ahmed, W.; Elhissi, A.; Khalid, N. R. Photocatalytic, Sonocatalytic and Sonophotocatalytic Degradation of Rhodamine B Using ZnO/CNTs Composites Photocatalysts. *Ultrason. Sonochem.* **2014**, *21*, 761.
- (12) Tahir, M. B.; Sohaib, M.; Sagir, M.; Rafique, M. Role of Nanotechnology in Photocatalysis. *Ref. Modul. Mater. Sci. Mater. Eng.* **2022**, *578*.
- (13) Gonçalves, C.; Bez Fontana, K.; Tenorio, M. A. R.; Bascuñan, V. L. A. F.; Lenzi, G. G.; Chaves, E. S. Zinc Oxide Immobilized on Alginate Beads as Catalyst for Photocatalytic Degradation of Textile Dyes — an Evaluation of Matrix Effects. *Desalin. Water Treat.* **2021**, *210*, 250–257.
- (14) Meshram, S. P.; Adhyapak, P. V.; Pardeshi, S. K.; Mulla, I. S.; Amalnerkar, D. P. Sonochemically Generated Cerium Doped ZnO Nanorods for Highly Efficient Photocatalytic Dye Degradation. *Powder Technol.* **2017**, *318*, 120–127.
- (15) Kabir, R.; Saifullah, M. A. K.; Ahmed, A. Z.; Masum, S. M.; Molla, M. A. I. Synthesis of N-Doped ZnO Nanocomposites for Sunlight Photocatalytic Degradation of Textile Dye Pollutants. *J. Compos. Sci.* **2020**, *4*, 49.
- (16) Yu, Z.; Zhang, L.; Wang, X.; He, D.; Suo, H.; Zhao, C. Fabrication of ZnO/Carbon Quantum Dots Composite Sensor for Detecting No Gas. *Sensors* **2020**, *20*, 4961.
- (17) Li, F.; Yang, D.; Xu, H. Non-Metal-Heteroatom-Doped Carbon Dots: Synthesis and Properties. *Chem. — A Eur. J.* **2019**, *25*, 1165–1176.
- (18) Kumar, M.; Ambika, S.; Hassani, A.; Nidheesh, P. V. Waste to Catalyst: Role of Agricultural Waste in Water and Wastewater Treatment. *Sci. Total Environ.* **2023**, *858*, No. 159762.
- (19) Hassani, A.; Eghbali, P.; Mahdipour, F.; Wacławek, S.; Lin, K. Y. A.; Ghanbari, F. Insights into the Synergistic Role of Photocatalytic Activation of Peroxymonosulfate by UVA-LED Irradiation over CoFe₂O₄-RGO Nanocomposite towards Effective Bisphenol A Degradation: Performance, Mineralization, and Activation Mechanism. *Chem. Eng. J.* **2023**, *453*, No. 139556.
- (20) Chen, J.; Shu, J.; Anqi, Z.; Juyuan, H.; Yan, Z.; Chen, J. Synthesis of Carbon Quantum Dots/TiO₂ Nanocomposite for Photo-Degradation of Rhodamine B and Cefradine. *Diamond Relat. Mater.* **2016**, *70*, 137–144.
- (21) Wang, Y.; Hu, A. Carbon Quantum Dots: Synthesis, Properties and Applications. *J. Mater. Chem. C* **2014**, *2*, 6921.
- (22) Ye, S. L.; Huang, J. J.; Luo, L.; Fu, H. J.; Sun, Y. M.; Shen, Y. D.; Lei, H. T.; Xu, Z. L. Preparation of Carbon Dots and Their Application in Food Analysis as Signal Probe. *Chin. J. Anal. Chem.* **2017**, *45*, 1571.
- (23) Mondal, S.; Yucknovsky, A.; Akulov, K.; Ghorai, N.; Schwartz, T.; Ghosh, H. N.; Amdursky, N. E. Efficient Photosensitizing Capabilities and Ultrafast Carrier Dynamics of Doped Carbon Dots. *J. Am. Chem. Soc.* **2019**, *141*, 15413–15422.
- (24) Das, G. S.; Tripathi, K. M.; Kumar, G.; Paul, S.; Mehara, S.; Bhowmik, S.; Pakhira, B.; Sarkar, S.; Roy, M.; Kim, T.; Korea, S.; Hall, D. Nitrogen-Doped Fluorescent Graphene Nanosheets as Visible-Light-Driven Photocatalysts for Dye Degradation and Selective Sensing of Ascorbic Acid. *New J. Chem.* **2019**, *43*, 14575.
- (25) Zhou, M.; Hu, Y.; Liu, Y.; Yang, W.; Qian, H. Microwave-Assisted Route to Fabricate Coaxial ZnO/C/CdS Nanocables with Enhanced Visible Light-Driven Photocatalytic Activity. *CrystEngComm* **2012**, *14*, 7686–7693.
- (26) Hassani, A.; Faraji, M.; Eghbali, P. Facile Fabrication of Mpg-C₃N₄/Ag/ZnO Nanowires/Zn Photocatalyst Plates for Photo-degradation of Dye Pollutant. *J. Photochem. Photobiol., A* **2020**, *400*, No. 112665.

- (27) Prabakaran, E.; Pillay, K. Synthesis of N-Doped ZnO Nanoparticles with Cabbage Morphology as a Catalyst for the Efficient Photocatalytic Degradation of Methylene Blue under UV and Visible Light. *RSC Adv.* **2019**, *9*, 7509–7535.
- (28) Atchudan, R.; Edison, T. N. J. I.; Mani, S.; Perumal, S.; Vinodh, R.; Thirunavukkarasu, S.; Lee, Y. R. Facile Synthesis of a Novel Nitrogen-Doped Carbon Dot Adorned Zinc Oxide Composite for Photodegradation of Methylene Blue. *Dalton Trans.* **2020**, *49*, 17725–17736.
- (29) Giri, S. K.; Mangaraj, S. Processing Influences on Composition and Quality Attributes of Soymilk and Its Powder. *Food Eng. Rev.* **2012**, *4*, 149.
- (30) Wellia, D. V.; Kusumawati, Y.; Diguna, L. J.; Amal, M. I. Introduction of Nanomaterials for Photocatalysis. In *Nanocomposites for Visible Light-Induced Photocatalysis*; Springer: Cham, 2017, pp. 1–17.
- (31) Gionco, C.; Fabbri, D.; Calza, P.; Paganini, M. C. Synthesis, Characterization, and Photocatalytic Tests of N-Doped Zinc Oxide: A New Interesting Photocatalyst. *J. Nanomater.* **2016**, *2016*, No. 4129864.
- (32) Muthulingam, S.; Bae, K.; Khan, R.; Lee, I. H.; Uthirakumar, P. Carbon Quantum Dots Decorated N-Doped ZnO: Synthesis and Enhanced Photocatalytic Activity on UV, Visible and Daylight Sources with Suppressed Photocorrosion. *J. Environ. Chem. Eng.* **2016**, *4*, 1148–1155.
- (33) Cheng, Y.; Bai, M.; Su, J.; Fang, C.; Li, H.; Chen, J.; Jiao, J. Synthesis of Fluorescent Carbon Quantum Dots from Aqua Mesophase Pitch and Their Photocatalytic Degradation Activity of Organic Dyes. *J. Mater. Sci. Technol.* **2019**, *35*, 1515–1522.
- (34) Loudhaief, N.; Labiadh, H.; Hannachi, E.; Zouaoui, M.; Salem, M. B. Synthesis of CdS Nanoparticles by Hydrothermal Method and Their Effects on the Electrical Properties of Bi-Based Superconductors. *J. Supercond. Novel Magn.* **2018**, *31*, 2305–2312.
- (35) Alarfaj, N. A.; El-Tohamy, M. F.; Oraby, H. F. CA 19-9 Pancreatic Tumor Marker Fluorescence Immunosensing Detection via Immobilized Carbon Quantum Dots Conjugated Gold Nanocomposite. *Int. J. Mol. Sci.* **2018**, *19*, 1162.
- (36) Tadesse, A.; Ramadevi, D.; Hagos, M.; Battu, G.; Basavaiah, K. Synthesis of Nitrogen Doped Carbon Quantum Dots/Magnetite Nanocomposites for Efficient Removal of Methyl Blue Dye Pollutant from Contaminated Water. *RSC Adv.* **2018**, *8*, 8528–8536.
- (37) Siriket, S.; Praoboon, N.; Kuimalee, S.; Phaisansuthichol, S.; Pookmanee, P.; Satienerakul, S. Synthesis of Highly Fluorescent Carbon Dots from Fermented Soya Bean Crisp for Determination of Mercuric Ions. *Maejo Int. J. Sci. Technol.* **2020**, *14*, 221–229.
- (38) Saengsrirachan, A.; Saikate, C.; Silasana, P.; Khemthong, P.; Wanmolee, W.; Phanthasri, J.; Youngjan, S.; Posoknistakul, P.; Ratchahat, S.; Laosiripojana, N.; Wu, K. C. W.; Sakdaronnarong, C. The Role of N and S Doping on Photoluminescent Characteristics of Carbon Dots from Palm Bunches for Fluorimetric Sensing of Fe³⁺ Ion. *Int. J. Mol. Sci.* **2022**, *23*, 5001.
- (39) Wang, S.; Sun, W.; Yang, D. S.; Yang, F. Soybean-Derived Blue Photoluminescent Carbon Dots. *Beilstein J. Nanotechnol.* **2020**, *11*, 606.
- (40) Wang, Y.; Hu, X.; Li, W.; Huang, X.; Li, Z.; Zhang, W.; Zhang, X.; Zou, X.; Shi, J. Preparation of Boron Nitrogen Co-Doped Carbon Quantum Dots for Rapid Detection of Cr(VI). *Spectrochim. Acta A Mol. Biomol. Spectrosc.* **2020**, *243*, No. 118807.
- (41) Zhang, Q.; Wang, R.; Feng, B.; Zhong, X.; Ostrikov, K. K. Photoluminescence Mechanism of Carbon Dots: Triggering High-Color-Purity Red Fluorescence Emission through Edge Amino Protonation. *Nat. Commun.* **2021**, *12*, 6856.
- (42) Petkova, P.; Vasilev, P.; Dimitrov, I. The Behaviour of Osmium Ions in the Tetrahedral Oxygen Coordination. *Bulg. Chem. Commun.* **2013**, *45*, 631–634.
- (43) Sarkar, S.; Banerjee, D.; Ghorai, U. K.; ChattoPadhyay, K. K. Hydrothermal Synthesis of Carbon Quantum Dots and Study of Its Photoluminescence Property. In *International Conference on Microelectronics, Computing and Communication, MicroCom*, 2016.
- (44) Yu, J.; Liu, C.; Yuan, K.; Lu, Z.; Cheng, Y.; Li, L.; Zhang, X.; Jin, P.; Meng, F.; Liu, H. Luminescence Mechanism of Carbon Dots by Tailoring Functional Groups for Sensing Fe³⁺ Ions. *Nanomaterials* **2018**, *8*, 233.
- (45) Xu, S.; Liu, Y.; Yang, H.; Zhao, K.; Li, J.; Deng, A. Fluorescent Nitrogen and Sulfur Co-Doped Carbon Dots from Casein and Their Applications for Sensitive Detection of Hg²⁺ and Biothiols and Cellular Imaging. *Anal. Chim. Acta* **2017**, *964*, 150.
- (46) Liu, C.; Zhang, F.; Hu, J.; Gao, W.; Zhang, M. A Mini Review on PH-Sensitive Photoluminescence in Carbon Nanodots. *Front. Chem.* **2020**, *8*, No. 605028.
- (47) Pirsaeheb, M.; Moradi, S.; Shahlaei, M.; Farhadian, N. Application of Carbon Dots as Efficient Catalyst for the Green Oxidation of Phenol: Kinetic Study of the Degradation and Optimization Using Response Surface Methodology. *J. Hazard. Mater.* **2018**, *353*, 444–453.
- (48) Prathumsuwan, T.; Jamnongsong, S.; Sampattavanich, S.; Paoprasert, P. Preparation of Carbon Dots from Succinic Acid and Glycerol as Ferrous Ion and Hydrogen Peroxide Dual-Mode Sensors and for Cell Imaging. *Opt. Mater.* **2018**, *86*, 517–529.
- (49) Longo, A. V.; Sciortino, A.; Cannas, M.; Messina, F. UV Photobleaching of Carbon Nanodots Investigated by: In Situ Optical Methods. *Phys. Chem. Chem. Phys.* **2020**, *22*, 13398–13407.
- (50) Longo, A. V.; Sciortino, A.; Cannas, M.; Messina, F. UV Photobleaching of Carbon Nanodots Investigated by: In Situ Optical Methods. *Phys. Chem. Chem. Phys.* **2020**, *22*, 13398.
- (51) Dsouza, S. D.; Buerkle, M.; Brunet, P.; Maddi, C.; Padmanaban, D. B.; Morelli, A.; Payam, A. F.; Maguire, P.; Mariotti, D.; Svrcek, V. The Importance of Surface States in N-Doped Carbon Quantum Dots. *Carbon N. Y.* **2021**, *183*, 1–11.
- (52) Dhenadhyalan, N.; Lin, K. C.; Saleh, T. A. Recent Advances in Functionalized Carbon Dots toward the Design of Efficient Materials for Sensing and Catalysis Applications. *Small* **2020**, *16*, No. 1905767.
- (53) Mintz, K. J.; Bartoli, M.; Rovere, M.; Zhou, Y.; Hettiarachchi, S. D.; Paudyal, S.; Chen, J.; Domena, J. B.; Liyanage, P. Y.; Sampson, R.; Khadka, D.; Pandey, R. R.; Huang, S.; Chusuei, C. C.; Tagliaferro, A.; Leblanc, R. M. A Deep Investigation into the Structure of Carbon Dots. *Carbon N. Y.* **2021**, *173*, 433–447.
- (54) Shaikh, A. F.; Tamboli, M. S.; Patil, R. H.; Bhan, A.; Ambekar, J. D.; Kale, B. B. Bioinspired Carbon Quantum Dots: An Antibiofilm Agents. *J. Nanosci. Nanotechnol.* **2019**, *19*, 2339–2345.
- (55) Eghbali, P.; Hassani, A.; Sündü, B.; Metin, Ö. *Strontium Titanate Nanocubes Assembled on Mesoporous Graphitic Catalytic Performance*. **2019**, *290*, 10–12. doi: [10.1016/j.molliq.2019.111208](https://doi.org/10.1016/j.molliq.2019.111208).
- (56) Goei, R.; Tan, F. T. F.; Ong, A. J.; Mandler, D.; Tok, A. I. Y. Development of Nitrogen-Decorated Carbon Dots (NCDs) Thermally Conductive Film for Windows Application. *Carbon Lett.* **2022**, *32*, 1065.
- (57) Liu, Y.; Jiang, H.; Liu, C.; Ge, Y.; Wang, L.; Zhang, B.; He, H.; Liu, S. Influence of Functional Groups on Toxicity of Carbon Nanomaterials. *Atmos. Chem. Phys.* **2019**, *19*, 8175.
- (58) Issa, M. A.; Abidin, Z. Z.; Sobri, S.; Rashid, S.; Mahdi, M. A.; Ibrahim, N. A.; Pudza, M. Y. Facile Synthesis of Nitrogen-Doped Carbon Dots from Lignocellulosic Waste. *Nanomaterials* **2019**, *9*, 1500.
- (59) Wu, P.; Li, W.; Wu, Q.; Liu, Y.; Liu, S. Hydrothermal Synthesis of Nitrogen-Doped Carbon Quantum Dots from Microcrystalline Cellulose for the Detection of Fe³⁺ Ions in an Acidic Environment. *RSC Adv.* **2017**, *7*, 44144–44153.
- (60) del Campo, A.; de Lucas-Gil, E.; Rubio-Marcos, F.; Arrieta, M. P.; Fernández-García, M.; Fernández, J. F.; Muñoz-Bonilla, A. Accelerated Disintegration of Compostable Ecovio Polymer by Using ZnO Particles as Filler. *Polym. Degrad. Stab.* **2021**, *185*, No. 109501.
- (61) Sagadevan, S.; Vennila, S.; Lett, J. A.; Marlinda, A. R.; Hamizi, N. A. B.; Johan, M. R. Tailoring the Structural, Morphological, Optical, Thermal and Dielectric Characteristics of ZnO Nanoparticles Using Starch as a Capping Agent. *Results Phys.* **2019**, *15*, No. 102543.
- (62) Magri, V. R.; Duarte, A.; Perotti, G. F.; Constantino, V. R. L. Investigation of Thermal Behavior of Layered Double Hydroxides Intercalated with Carboxymethylcellulose Aiming Bio-Carbon Based Nanocomposites. *ChemEngineering* **2019**, *3*, 55.

- (63) Elmorsi, T. M.; Elsayed, M. H.; Bakr, M. F. Enhancing the Removal of Methylene Blue by Modified ZnO Nanoparticles: Kinetics and Equilibrium Studies. *Can. J. Chem.* **2017**, *95*, 590–600.
- (64) Zhang, X.; Jiang, M.; Niu, N.; Chen, Z.; Li, S.; Liu, S.; Li, J. Natural-Product-Derived Carbon Dots: From Natural Products to Functional Materials. *ChemSusChem* **2018**, *11*, 11–24.
- (65) He, B.; Li, Z.; Zhao, D.; Liu, H.; Zhong, Y.; Ning, J.; Zhang, Z.; Wang, Y.; Hu, Y. Fabrication of Porous Cu-Doped BivO₄ Nanotubes as Efficient Oxygen-Evolving Photocatalysts. *ACS Appl. Nano Mater.* **2018**, *1*, 2589–2599.
- (66) Kaur, M.; Kumar, V.; Kaur, P.; Sharma, R. Effect of Synthesis Methods on Dielectric Performance of ZnO Nanoparticles. *Mater. Technol.* **2022**, *37*, 1156–1167.
- (67) Farha, A. H.; Al Naim, A. F.; Mazher, J.; Nasr, O.; Alouane, M. H. Structural and Optical Characteristics of Highly UV-Blue Luminescent ZnO Nanoparticles Prepared by Sol-Gel Method. *Materials* **2020**, *13*, 879.
- (68) Beltrán, J. J.; Barrero, C. A.; Punnoose, A. Understanding the Role of Iron in the Magnetism of Fe Doped ZnO Nanoparticles. *Phys. Chem. Chem. Phys.* **2015**, *17*, 15284–15296.
- (69) Kaur, M.; Kumar, V.; Singh, J.; Datt, J.; Sharma, R. Effect of Cu-N Co-Doping on the Dielectric Properties of ZnO Nanoparticles. *Mater. Technol.* **2022**, *37*, 2644–2658.
- (70) Muthulingam, S.; Lee, I. H.; Uthirakumar, P. Highly Efficient Degradation of Dyes by Carbon Quantum Dots/N-Doped Zinc Oxide (CQD/N-ZnO) Photocatalyst and Its Compatibility on Three Different Commercial Dyes under Daylight. *J. Colloid Interface Sci.* **2015**, *455*, 101–109.
- (71) Liang, H.; Tai, X.; Du, Z.; Yin, Y. Enhanced Photocatalytic Activity of ZnO Sensitized by Carbon Quantum Dots and Application in Phenol Wastewater. *Opt. Mater.* **2020**, *100*, No. 109674.
- (72) Li, Y.; Liao, C. Recent Advances in Zinc Oxide Nanostructures with Antimicrobial Activities. *Int. J. Mol. Sci.* **2020**, *21*, 8836.
- (73) Anandan, S.; Muthukumar, S.; Ashokkumar, M. Structural and Optical Properties of Y, Cu Co-Doped ZnO Nanoparticles by Sol-Gel Method. *Superlattices Microstruct.* **2014**, *74*, 247–260.
- (74) Gupta, R.; Krishnarao Eswar, N.; Modak, J. M.; Madras, G. Visible Light Driven Efficient N and Cu Co-Doped ZnO for Photoinactivation of: Escherichia Coli. *RSC Adv.* **2016**, *6*, 85675–85687.
- (75) Joshi, K.; Rawat, M.; Gautam, S. K.; Singh, R. G.; Ramola, R. C.; Singh, F. Band Gap Widening and Narrowing in Cu-Doped ZnO Thin Films. *J. Alloys Compd.* **2016**, *680*, 252–258.
- (76) Janotti, A.; Van De Walle, C. G. Oxygen Vacancies in ZnO. *Appl. Phys. Lett.* **2005**, *87*, 122102.
- (77) Janotti, A.; Van De Walle, C. G. New Insights into the Role of Native Point Defects in ZnO. *J. Cryst. Growth* **2006**, *287*, 58–65.
- (78) Janotti, A.; Van De Walle, C. G. Native Point Defects in ZnO. *Phys. Rev. B Condens. Matter Mater. Phys.* **2007**, *76*, No. 165202.
- (79) Zhang, S. B.; Wei, S. H.; Zunger, A. Intrinsic N-Type versus p-Type Doping Asymmetry and the Defect Physics of ZnO. *Phys. Rev. B Condens. Matter Mater. Phys.* **2001**, *63*, No. 075205.
- (80) Oba, F.; Togo, A.; Tanaka, I.; Paier, J.; Kresse, G. Defect Energetics in ZnO: A Hybrid Hartree-Fock Density Functional Study. *Phys. Rev. B Condens. Matter Mater. Phys.* **2008**, *77*, No. 245202.
- (81) Oba, F.; Choi, M.; Togo, A.; Tanaka, I. Point Defects in ZnO: An Approach from First Principles. *Sci. Technol. Adv. Mater.* **2011**, *12*, No. 034302.
- (82) Paudel, T. R.; Lambrecht, W. R. L. First-Principles Calculation of the O Vacancy in ZnO: A Self-Consistent Gap-Corrected Approach. *Phys. Rev. B Condens. Matter Mater. Phys.* **2008**, *77*, No. 205202.
- (83) Ni, M.; Zhang, H.; Khan, S.; Chen, X.; Chen, F.; Guo, C.; Zhong, Y.; Hu, Y. In-Situ Photodeposition of Cadmium Sulfide Nanocrystals on Manganese Dioxide Nanorods with Rich Oxygen Vacancies for Boosting Water-to-Oxygen Photooxidation. *J. Colloid Interface Sci.* **2022**, *613*, 764–774.
- (84) Qin, F.; Nikolaev, S. A.; Suwardi, A.; Wood, M.; Zhu, Y.; Tan, X.; Aydemir, U.; Ren, Y.; Yan, Q.; Hu, L.; Snyder, G. J. Crystal Structure and Atomic Vacancy Optimized Thermoelectric Properties in Gadolinium Selenides. *Chem. Mater.* **2020**, *32*, 10130–10139.
- (85) Sasinska, A.; Bialuschewski, D.; Islam, M. M.; Singh, T.; Deo, M.; Mathur, S. Experimental and Theoretical Insights into Influence of Hydrogen and Nitrogen Plasma on the Water Splitting Performance of ALD Grown TiO₂ Thin Films. *J. Phys. Chem. C* **2017**, *121*, 15538–15548.
- (86) Lynch, J.; Giannini, C.; Cooper, J. K.; Loiudice, A.; Sharp, I. D.; Buonsanti, R. Substitutional or Interstitial Site Selective Nitrogen Doping in TiO₂ Nanostructures. *J. Phys. Chem. C* **2015**, *119*, 7443–7452.
- (87) Pearson, R. G. Absolute Electronegativity and Hardness: Application to Inorganic Chemistry. *Inorg. Chem.* **1988**, *27*, 734–740.
- (88) Wang, B.; Wang, X.; Lu, L.; Zhou, C.; Xin, Z.; Wang, J.; Ke, X. K.; Sheng, G.; Yan, S.; Zou, Z. Oxygen-Vacancy-Activated CO₂ Splitting over Amorphous Oxide Semiconductor Photocatalyst. *ACS Catal.* **2018**, *8*, 516–525.
- (89) Velumani, A.; Sengodan, P.; Arumugam, P.; Rajendran, R.; Santhanam, S.; Palanisamy, M. Carbon Quantum Dots Supported ZnO Sphere Based Photocatalyst for Dye Degradation Application. *Curr. Appl. Phys.* **2020**, *20*, 1176–1184.
- (90) Das, G. S.; Shim, J. P.; Bhatnagar, A.; Tripathi, K. M.; Kim, T. Y. Biomass-Derived Carbon Quantum Dots for Visible-Light-Induced Photocatalysis and Label-Free Detection of Fe(III) and Ascorbic Acid. *Sci. Rep.* **2019**, *9*, 15084.
- (91) Liang, H.; Tai, X.; Du, Z.; Yin, Y. Enhanced Photocatalytic Activity of ZnO Sensitized by Carbon Quantum Dots and Application in Phenol Wastewater. *Opt. Mater.* **2020**, *100*, No. 109674.
- (92) Jayanthi, K.; Chawla, S.; Chhikara, M. Dopant Induced Morphology Changes in ZnO Nanocrystals. *Appl. Surf. Sci.* **2009**, *255*, 5869.
- (93) Atchudan, R.; Edison, T. N. J. L.; Perumal, S.; Karthik, N.; Karthikeyan, D.; Shanmugam, M.; Lee, Y. R. Concurrent Synthesis of Nitrogen-Doped Carbon Dots for Cell Imaging and ZnO@nitrogen-Doped Carbon Sheets for Photocatalytic Degradation of Methylene Blue. *J. Photochem. Photobiol., A* **2018**, *350*, 75–85.
- (94) Gao, D.; Zhao, P. Carbon Quantum Dots Decorated on ZnO Nanoparticles: An Efficient Visible-Light Responsive Antibacterial Agents. *Appl. Organomet. Chem.* **2020**, *34*, No. e5665.
- (95) Long, L.; Wu, Q.; Chao, Q.; Dong, Y.; Wu, L.; Zhang, Q.; Zhou, Y.; Wang, D. Surface-State-Mediated Interfacial Charge Dynamics between Carbon Dots and ZnO toward Highly Promoting Photocatalytic Activity. *J. Chem. Phys.* **2020**, *153*, No. 044708.
- (96) Li, J.; Liu, K.; Xue, J.; Xue, G.; Sheng, X.; Wang, H.; Huo, P.; Yan, Y. CQDS Preluded Carbon-Incorporated 3D Burger-like Hybrid ZnO Enhanced Visible-Light-Driven Photocatalytic Activity and Mechanism Implication. *J. Catal.* **2019**, *369*, 450–461.
- (97) Cabrera German, D.; Gomez, A. H. Detailed Peak Fitting Analysis of the Zn 2 p Photoemission Spectrum for Metallic Films and Its Initial Oxidation Stages. *Surf. Interface Anal.* **2017**, *49*, 1078–1087.
- (98) Li, Q.; Li, H.; Wang, R.; Li, G.; Yang, H.; Chen, R. Controllable Microwave and Ultrasonic Wave Combined Synthesis of ZnO Micro-/Nanostructures in HEPES Solution and Their Shape-Dependent Photocatalytic Activities. *J. Alloys Compd.* **2013**, *567*, 1–9.
- (99) Wang, Y.; Yan, L.; Ji, G.; Wang, C.; Gu, H.; Luo, Q.; Chen, Q.; Chen, L.; Yang, Y.; Ma, C. Q.; Liu, X. Synthesis of N,S-Doped Carbon Quantum Dots for Use in Organic Solar Cells as the ZnO Modifier to Eliminate the Light-Soaking Effect. *ACS Appl. Mater. Interfaces* **2019**, *11*, 2243–2253.
- (100) Rajender, G.; Giri, P. K. Formation Mechanism of Graphene Quantum Dots and Their Edge State Conversion Probed by Photoluminescence and Raman Spectroscopy. *J. Mater. Chem. C* **2016**, *4*, 10852–10865.
- (101) Wu, W. T.; Shi, L.; Zhu, Q.; Wang, Y.; Xu, G.; Pang, W. N-Doped ZnO Nano-Arrays: A Facile Synthesis Route, Characterization and Photoluminescence. *Mater. Lett.* **2007**, *61*, 4752–4755.
- (102) Suwannaruang, T.; Kamonsuangkasem, K.; Kidkhunthod, P.; Chirawatkul, P.; Saiyasombat, C.; Chanlek, N.; Wantala, K. Influence of Nitrogen Content Levels on Structural Properties and Photocatalytic

Activities of Nanorice-like N-Doped TiO₂ with Various Calcination Temperatures. *Mater. Res. Bull.* **2018**, *105*, 265–276.

(103) Silva, I. M. P.; Byzinski, G.; Ribeiro, C.; Longo, E. Different Dye Degradation Mechanisms for ZnO and ZnO Doped with N (ZnO:N). *J. Mol. Catal. A: Chem.* **2016**, *417*, 89–100.

(104) Ievtushenko, A.; Khyzhun, O.; Shtepliuk, I.; Tkach, V.; Lazorenko, V.; Lashkarev, G. X-Ray Photoelectron Spectroscopy Study of Nitrogen and Aluminum-Nitrogen Doped ZnO Films. *Acta Phys. Pol. A* **2013**, *124*, 858–861.

(105) Barnes, T. M.; Leaf, J.; Hand, S.; Fry, C.; Wolden, C. A. A Comparison of Plasma-Activated N₂/O₂ and N₂O/O₂ Mixtures for Use in ZnO:N Synthesis by Chemical Vapor Deposition. *J. Appl. Phys.* **2004**, *96*, 7036–7044.

(106) Chiesa, M.; Livraghi, S.; Paganini, M. C.; Salvadori, E.; Giamello, E. Nitrogen-Doped Semiconducting Oxides. Implications on Photochemical, Photocatalytic and Electronic Properties Derived from EPR Spectroscopy. *Chem. Sci.* **2020**, *11*, 6623–6641.

(107) Park, C. H.; Zhang, S. B.; Wei, S. H. Origin of P-Type Doping Difficulty in ZnO: The Impurity Perspective. *Phys. Rev. B Condens. Matter Mater. Phys.* **2002**, *66*, No. 073202.

(108) Rahman, M. M.; Shafiullah, A. Z.; Pal, A.; Islam, M. A.; Jahan, I.; Saha, B. B. Study on Optimum Iupac Adsorption Isotherm Models Employing Sensitivity of Parameters for Rigorous Adsorption System Performance Evaluation. *Energies* **2021**, *14*, 7478.

(109) Jadhav, N. A.; Singh, P. K.; Rhee, H. W.; Bhattacharya, B. Effect of Variation of Average Pore Size and Specific Surface Area of ZnO Electrode (WE) on Efficiency of Dye-Sensitized Solar Cells. *Nanoscale Res. Lett.* **2014**, *9*, 575.

(110) Ni, M.; Zhang, H.; Khan, S.; Chen, X.; Chen, F.; Guo, C.; Zhong, Y.; Hu, Y. In-Situ Photodeposition of Cadmium Sulfide Nanocrystals on Manganese Dioxide Nanorods with Rich Oxygen Vacancies for Boosting Water-to-Oxygen Photooxidation. *J. Colloid Interface Sci.* **2022**, *613*, 764–774.

(111) Li, C.; Wu, H.; Zhu, D.; Zhou, T.; Yan, M.; Chen, G.; Sun, J.; Dai, G.; Ge, F.; Dong, H. High-Efficient Charge Separation Driven Directionally by Pyridine Rings Grafted on Carbon Nitride Edge for Boosting Photocatalytic Hydrogen Evolution. *Appl. Catal. B Environ.* **2021**, *297*, No. 120433.

(112) Roza, L.; Fauzia, V.; Rahman, M. Y. A.; Isnaeni, I.; Putro, P. A. ZnO Nanorods Decorated with Carbon Nanodots and Its Metal Doping as Efficient Photocatalyst for Degradation of Methyl Blue Solution. *Opt. Mater.* **2020**, *109*, No. 110360.

(113) Che, H.; Liu, C.; Che, G.; Liao, G.; Dong, H.; Li, C.; Song, N.; Li, C. Facile Construction of Porous Intramolecular G-C₃N₄-Based Donor-Acceptor Conjugated Copolymers as Highly Efficient Photocatalysts for Superior H₂ Evolution. *Nano Energy* **2020**, *67*, No. 104273.

(114) Sharma, S.; Mehta, S. K.; Kansal, S. K. N Doped ZnO/C-Dots Nanoflowers as Visible Light Driven Photocatalyst for the Degradation of Malachite Green Dye in Aqueous Phase. *J. Alloys Compd.* **2017**, *699*, 323–333.

(115) Song, S.; Wu, K.; Wu, H.; Guo, J.; Zhang, L. Multi-Shelled ZnO Decorated with Nitrogen and Phosphorus Co-Doped Carbon Quantum Dots: Synthesis and Enhanced Photodegradation Activity of Methylene Blue in Aqueous Solutions. *RSC Adv.* **2019**, *9*, 7362–7374.

(116) Sodeifian, G.; Behnood, R. Hydrothermal Synthesis of N-Doped GQD/CuO and N-Doped GQD/ZnO Nanophotocatalysts for MB Dye Removal Under Visible Light Irradiation: Evaluation of a New Procedure to Produce N-Doped GQD/ZnO. *J. Inorg. Organomet. Polym. Mater.* **2020**, *30*, 1266–1280.

(117) Bolton, J. R.; Bircher, K. G.; Tumas, W.; Tolman, C. A. Figures-of-Merit for the Technical Development and Application of Advanced Oxidation Technologies for Both Electric- and Solar-Driven Systems. *Pure Appl. Chem.* **2001**, *73*, 627–637.

(118) Ayad, M. M.; El-Nasr, A. A. Adsorption of Cationic Dye (Methylene Blue) from Water Using Polyaniline Nanotubes Base. *J. Phys. Chem. C* **2010**, *114*, 14377–14383.

(119) Gaya, U. I.; Abdullah, A. H.; Zainal, Z.; Hussein, M. Z. Photocatalytic Treatment of 4-Chlorophenol in Aqueous ZnO

Suspensions: Intermediates, Influence of Dosage and Inorganic Anions. *J. Hazard. Mater.* **2009**, *168*, 57–63.

(120) Zhang, J.; Liu, Q.; He, H.; Shi, F.; Huang, G.; Xing, B.; Jia, J.; Zhang, C. Coal Tar Pitch as Natural Carbon Quantum Dots Decorated on TiO₂ for Visible Light Photodegradation of Rhodamine B. *Carbon N. Y.* **2019**, *152*, 284–294.